



# Generation of Kappa Distributions in Solar Wind at 1 au

G. Livadiotis<sup>1</sup> M. I. Desai<sup>1,2</sup> and L. B. Wilson, III<sup>3</sup>

<sup>1</sup> Southwest Research Institute, San Antonio, TX, USA; [givadiotis@swri.edu](mailto:givadiotis@swri.edu)

<sup>2</sup> University of Texas at San Antonio, Department of Physics & Astronomy, San Antonio, TX, USA

<sup>3</sup> NASA Goddard Space Flight Center, Greenbelt, MD, USA

Received 2017 September 24; revised 2017 December 8; accepted 2018 January 9; published 2018 February 1

## Abstract

We examine the generation of kappa distributions in the solar wind plasma near 1 au. Several mechanisms are mentioned in the literature, each characterized by a specific relationship between the solar wind plasma features, the interplanetary magnetic field (IMF), and the kappa index—the parameter that governs the kappa distributions. This relationship serves as a signature condition that helps the identification of the mechanism in the plasma. In general, a mechanism that generates kappa distributions involves a single or a series of stochastic or physical processes that induces local correlations among particles. We identify three fundamental solar wind plasma conditions that can generate kappa distributions, noted as (i) Debye shielding, (ii) frozen IMF, and (iii) temperature fluctuations, each one prevailing in different scales of solar wind plasma and magnetic field properties. Moreover, our findings show that the kappa distributions, and thus, their generating mechanisms, vary significantly with solar wind features: (i) the kappa index has different dependence on the solar wind speed for slow and fast modes, i.e., slow wind is characterized by a quasi-constant kappa index,  $\kappa \approx 4.3 \pm 0.7$ , while fast wind exhibits kappa indices that increase with bulk speed; (ii) the dispersion of magnetosonic waves is more effective for lower kappa indices (i.e., further from thermal equilibrium); and (iii) the kappa and polytropic indices are positively correlated, as it was anticipated by the theory.

**Key words:** methods: analytical – methods: statistical – Sun: heliosphere – plasmas

## 1. Introduction

Non-Maxwellian particle velocity distributions are ubiquitously observed in collisionless space plasmas such as the solar wind. Measurements confirmed by many missions show enhanced particle populations of suprathermal tails that cannot be described by classical Maxwellian distributions. These are better approximated by kappa distributions or combinations thereof. Classical particle systems in thermal equilibrium have their phase-space distribution stabilized into a Maxwell–Boltzmann function. These systems are characterized by limited or zero correlations among the velocities or energies of their particles. In contrast, space plasmas are particle systems frequently described by stationary states out of thermal equilibrium, namely, their distributions are stabilized into a function that is not given by the Maxwell–Boltzmann formulation, and is typically described by kappa distributions (e.g., see the book Livadiotis 2017, and the reviews of Pierrard & Lazar 2010; Livadiotis & McComas 2013a; Livadiotis 2015a). These systems are characterized by long-range interactions that induce correlations resulting to a collective behavior among particles (e.g., see Jund et al. 1995; Salazar & Toral 1999; Villain 2008; Tsallis 2009; Grassi 2010; Tirkakli & Borges 2016).

Kappa distributions were employed in order to describe numerous space plasma populations in the heliosphere, from solar wind and the planetary magnetospheres to the inner heliosheath and beyond (for solar wind, see, e.g., Collier et al. 1996; Maksimovic et al. 1997; Pierrard et al. 1999; Mann et al. 2002; Marsch 2006; Zouganelis 2008; Štverák et al. 2009; Livadiotis & McComas 2010a; Yoon et al. 2012; Fuselier et al. 2014; Yoon 2014; Pierrard & Pieters 2015; Pavlos et al. 2016; for other space plasmas, see Livadiotis 2017, Chapter 1.2).

Kappa distributions have become increasingly widespread across space physics, with an exponential growth of the

relevant papers (e.g., Livadiotis & McComas 2009, 2013a; Livadiotis 2015a, 2017, Chapter 1). However, the majority of these papers refer to various applications of kappa distributions in space plasmas. To date, there is no systematic analysis for verifying the origin of kappa distributions in solar wind.

Recently, we have shown that the kappa index (the parameter that labels and governs kappa distributions) is correlated with other solar wind plasma parameters (e.g., density  $n$ , temperature  $T$ ) (Livadiotis 2015a). These trends revealed non-universal relationships that vary with location, time, and the type of space plasmas. In Figures 1 and 2 of that paper, we illustrated the representative values of density  $n$ , temperature  $T$ , and kappa index  $\kappa$  of  $\sim 40$  different space plasmas. We also plotted the quantity  $M = 1/(\kappa - 0.5)$ , which provides a measure of how far the system resides from thermal equilibrium (Livadiotis & McComas 2010a, 2010b), showing that  $M$  is negatively correlated (or,  $\kappa$  is positively correlated) with  $T$  and  $n$ ; on average,  $M$  is linearly decreasing as  $M \approx 2.27 - 0.19 \cdot \log(nT^{0.6})$ . Similar relationships between kappa index and temperature have also been observed in individual space plasmas, e.g., the magnetosheath (Ogasawara et al. 2013) or the inner heliosheath (Livadiotis et al. 2011, 2012, 2013). Aside from the temperature and density, the kappa index was also found to be connected with other plasma parameters, e.g., polytropic index (e.g., Meyer-Vernet et al. 1995; Livadiotis 2017, Chapter 5), thermal pressure (Livadiotis & McComas 2012), potential energy (Ogasawara et al. 2017), and magnetic field. The latter has significant interplay in the generation of kappa distributions in space plasmas, where the kappa index is found to decrease as the magnetic field strength increases (e.g., see Ogasawara et al. 2013; Tao & Lu 2014; Stepanova & Antonova 2015).

The frequently observed trends between the kappa index and other space plasma parameters can be caused by mechanisms

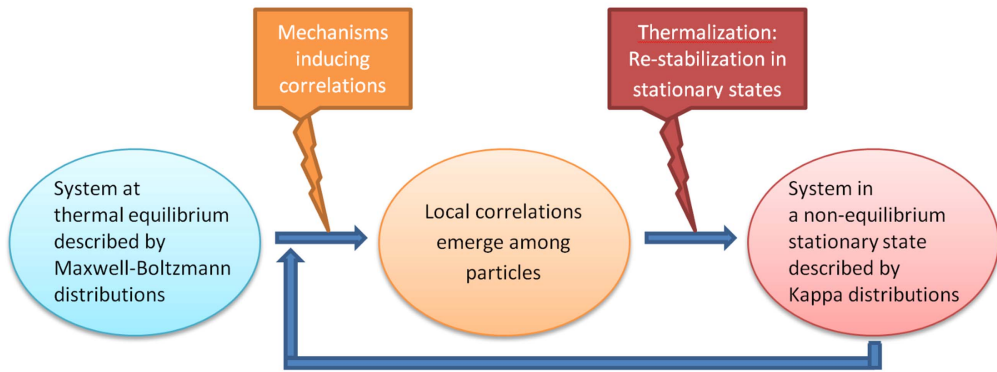


**Figure 1.** General scheme of mechanisms generating kappa distributions: Correlation and Thermalization. The input can be systems at thermal equilibrium described by Maxwell–Boltzmann distributions or systems in some initial stationary state described by kappa distributions.

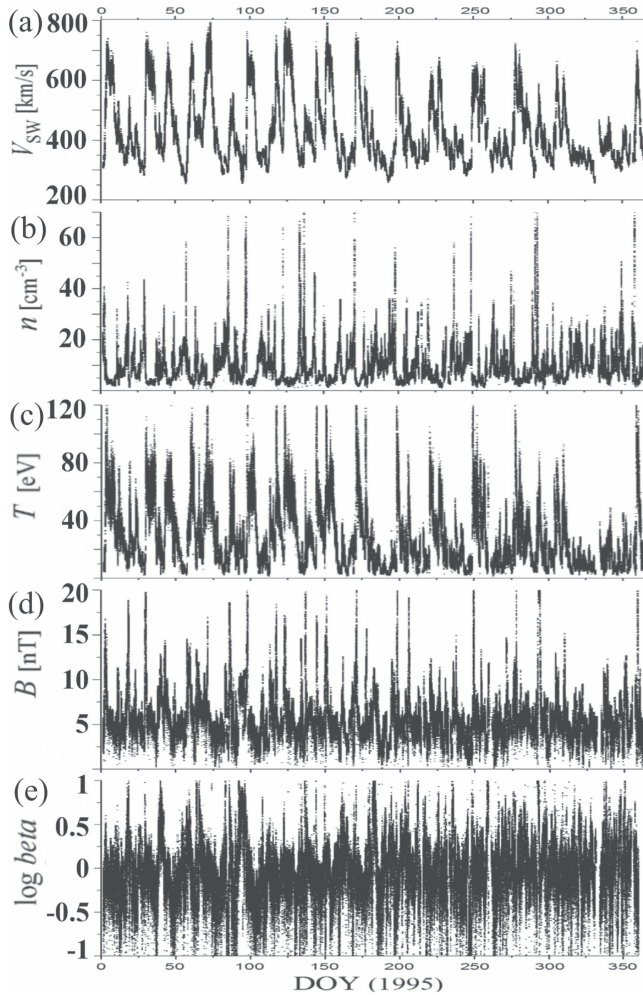


**Figure 2.**  $\sim 92$  s resolution measurements of bulk solar wind plasma moments (speed  $V_{\text{sw}}$ , density  $n$ , temperature  $T$ ) and magnetic field magnitude  $B$  (and plasma beta  $\beta$ , i.e., the ratio of the thermal to magnetic pressure), recorded, respectively, from SWE and MAG onboard *Wind* during the year 1995. The temperature is deduced from the thermal speed,  $V_{\text{th}} = (k_{\text{B}}T/m_i)^{1/2}$ .

responsible for generating kappa distributions. There are various mechanisms mentioned in the literature that can generate kappa distributions, and thus, produce relationships among the kappa index and other plasma parameters. Some examples are studied in Livadiotis (2017), that is, the connection with polytropes (Chapter 5; Livadiotis 2016), superstatistics (Chapter 6; Beck & Cohen 2003), the presence

of weak turbulence (Chapter 8; Yoon 2014), the effect of pickup ions especially in the inner heliosheath (Chapter 10; Livadiotis & McComas 2011a), the pump acceleration mechanism (Chapter 15; Fisk & Gloeckler 2014,), and the effect of shock waves (Chapter 16; Zank et al. 2006).

The paper focuses on three plasma conditions that can be applied to solar wind near 1 au: (i) Debye shielding, (ii) frozen interplanetary magnetic field (IMF), and (iii) temperature fluctuations; (see Section 2). Each of these conditions indicates a specific relationship of the kappa index with the space plasma parameters and/or the magnetic field. Such a relationship serves as a signature that helps the identification of the generating mechanism. In this analysis, we utilize multiple 1 au solar wind plasma and magnetic field data sets, taken from *Wind* observations, to study the coupling between the kappa index, the solar wind plasma parameters, and the IMF, and ultimately, to advance our understanding of the underlying plasma conditions that generate kappa distributions in the solar wind near 1 au. In Section 2, we develop the general theory of mechanisms that can generate kappa distributions in space plasmas, which is based on the concept of particle correlations; then, the case of the three conditions that are interwoven with the generation of kappa distributions are developed. In Section 3, we describe the methodology for deriving the kappa indices. In Section 4, we present the results of the analyses that (1) determine the properties of the kappa distributions (kappa indices) that characterize the solar wind plasma at 1 au and (2) detect any relationships between the bulk solar wind properties (speed, temperature, density, etc.), IMF, and the derived kappa indices. In Section 5, we distinguish the kappa-plasma-magnetic field relationships and identify the three conditions, theoretically developed in Section 2. Then, we show and discuss how the kappa distributions (and their generating mechanisms) vary with the solar wind features. Specifically, we examine the following: (i) the variation between slow and fast solar wind modes, (ii) the dispersion of fast magnetosonic waves, and (iii) the connection with polytropes. Section 6 summarizes the conclusions, and finally, we provide two appendices to help the comprehension of systematic and statistical errors: Appendix A provides the error estimation analysis of (1) the parameters involved in the technique of deriving the kappa indices, (2) the temperature fluctuations, and (3) the plasma beta parameter; Appendix B shows that the contribution of other ion populations in the derivation of proton temperature and its error is insignificant, and thus can be ignored.

## 2. Theory

### 2.1. Thermalized Particle Systems that Have Correlations are Described by Kappa Distributions

Systems with no correlations between their particles are stabilized into thermal equilibrium—the state where any flow of heat is in balance. Such systems have their distribution functions of velocities stabilized into Maxwell–Boltzmann distributions. However, totally uncorrelated systems are a physically unattainable limit, because even if the particles were uncorrelated prior to a collision as assumed by Boltzmann’s “molecular chaos” (Stosszahl Ansatz), their velocities after the collision are no longer truly uncorrelated. For the opposite limit, every particle is correlated to all the other particles of a system. In all real physical systems, particles have some level of correlation with each other, and the phase-space distributions can be very complicated. That is, in general, the particles of a physical system are neither fully correlated nor fully uncorrelated to the other particles of the system.

Due to particle correlations, systems reside in stationary states out of thermal equilibrium; namely, there is not just the unique stationary state of thermal equilibrium described by the classical Maxwell–Boltzmann distribution, but an infinite number of stationary states described by kappa distributions; the kappa index is inversely proportional to the correlation coefficient  $\rho$  between the energies of any two particles,  $\kappa = (3/2)/\rho$  (Abe 1999; Livadiotis & McComas 2011b; Livadiotis 2015b). The largest kappa index is infinity, corresponding to the system residing at thermal equilibrium, where the particles are characterized by zero correlation ( $\rho = 0$ ). The smallest kappa index is 3/2 (for 3D distributions), corresponding to the furthest state from thermal equilibrium, called anti-equilibrium, where the particles have the highest correlation ( $\rho = 1$ ). All other cases reside between these extremes, with kappa indices between 3/2 and  $\infty$ , i.e., with correlation  $\rho$  between 0 and 1.

Therefore, local correlations among the velocities or energies of particles are interwoven with kappa distributions. (As explained above, the covariance or correlation coefficient between the energies of any two particles is non-zero for finite values of the kappa index.) When investigating for mechanisms generating kappa distributions, we are actually searching for mechanisms generating correlations. Once correlations are generated, then, distributions are re-thermalized, i.e., they are assigned with a temperature. The only known stationary distributions assigned with a temperature are the kappa distributions (or combinations/superposition thereof).

This must be stressed out again: the existence of particle stationary states characterized by both (i) temperature and (ii) correlations means necessarily the formation of kappa distributions (or combinations thereof). Particle systems, with or without correlations, may exist in other formulations but they will not be characterized by a physically meaningful temperature that follows the thermodynamic laws. (This was first shown by Abe 2002; any particle system obeying the zeroth law of thermodynamics is described by the entropy associated with kappa distributions.) Therefore, a mechanism generating local correlations among particles in a system residing in a stationary state is actually a mechanism generating kappa distributions.

A mechanism that generates kappa distributions involves a single or a series of stochastic or physical processes that induces

local correlations among particles. The general scheme that characterizes these mechanisms is based on the concept of particle correlations, and is composed of two parts: (1) generation of local correlations among particles and (2) “thermalization,” that is, the re-stabilization of the particle system into a nonequilibrium stationary state assigned by a temperature, and thus, described by kappa distributions (Figure 1).

### 2.2. Three Basic Plasma Conditions Generating Kappa Distributions in Solar Wind Near 1 au

Here we examine three plasma conditions suitable for generating kappa distributions in the solar wind plasma, and study their characteristic relationships between the bulk solar wind properties (speed, temperature, density, etc.), the IMF, and the kappa index.

Space plasmas, such as the solar wind, are collisionless (the particle coupling due to collisions is negligible), and show strong collective behavior, mainly owing to the particle correlations induced by the following causes: (i) *Debye shielding* that correlates particles within a Debye sphere (Livadiotis & McComas 2014a); (ii) *frozen IMF*, that is, the presence of a magnetic field, by itself, induces correlations between particles; the coupling between plasma constituents and the embedded magnetic field occurring on various temporal and spatial scales “binds” particles together (e.g., Kivelson & Russell 1995, Chapter 5.2, p.136); and (iii) *temperature fluctuations*, a statistical process that correlates particles (Beck & Cohen 2003; Schwadron et al. 2010; Livadiotis 2017, Chapter 6). These plasma conditions constitute three abstract mechanisms that can generate kappa distributions in solar wind near 1 au (Table 1):

(i) *Debye shielding*: Debye shielding produces a natural ordering of particle correlations in plasmas (e.g., Livadiotis & McComas 2013b, 2014b). Inside a Debye sphere, particles are highly correlated with each other through their electromagnetic interactions. In contrast, at distances greater than a Debye length  $\lambda_D$ , particles are largely uncorrelated owing to the Debye shielding of the closer particles. Indeed, as shown in (Livadiotis & McComas 2014a), within the Debye sphere, the long-range potential energy that bounds and thus correlates the particles together, prevails the thermal energy that de-organizes the motions of particles, destroying their correlations; beyond the Debye sphere, the thermal energy dominates the potential energy and the correlations are practically dissolved. The distance at which the two energies become equivalent reads the Debye length; it actually provides one of the main interpretations (definitions) of the Debye length (Kallenrode 2004; Baumjohann & Treumann 2012; Livadiotis & McComas 2014a).

Therefore, each Debye sphere represents a cluster of correlated particles (ions and electrons), which is essentially uncorrelated with the more distant particles and their Debye spheres. In this structuring of particle distributions, clusters share no substantial interaction and behave like essentially uncorrelated phase-space elements of the plasma. Particles within a cluster are correlated with each other, but they are essentially uncorrelated with other particles beyond the correlation cluster (Debye sphere). Weakly coupled plasmas have small coupling parameter  $\Gamma$ , defined by the ratio of the electrostatic potential energy at

**Table 1**  
Plasma Conditions—Mechanisms for Generating Kappa Distributions in Solar Wind Near 1 au

Mechanism	Key Parameter	Relationship with Kappa Index
Debye shielding	Debye Number $N_D$	$\kappa$ negatively correlated with $N_D$
Magnetic field binding	Plasma beta $\beta$	$\kappa$ positively correlated with $\beta$
Temperature fluctuations	Temperature variation $\delta T^2$	$\kappa$ negatively correlated with $\delta T^2$

**Note.** The positive/negative *correlations* between the data of the kappa index and the key parameters (that is, their correspondence) must not be confused with the *correlations* between particles involved in the generation of kappa distributions, according to the scheme of Figure 1.

the interparticle or Wigner–Seitz radius over the kinetic energy; equivalently, they have a large number of particles within their Debye spheres,  $N_D = (4\pi/3)n\lambda_D^3$  (the Debye number), because of the relation  $\Gamma \cong 0.1 \cdot N_D^{-2/3}$ . Also, a large Debye number  $N_D$  leads to large mean-free-path,  $L_m \propto \lambda_D N_D$ . Hence, weakly coupled plasmas ( $\Gamma \ll 1$  or  $N_D \gg 1$ ) are equivalent to collisionless plasmas ( $L_m \gg \lambda_D$ ). Thus, local correlations among particles within the Debye spheres can persist for a substantial length of time without being destroyed by collisions. The larger the Debye number  $N_D$ , the more effective the collective behavior in plasma, which inclines the system even further from thermal equilibrium; thus, the smaller the kappa index becomes. Hence,  $N_D$  is *negatively correlated with  $\kappa$* .

(ii) *Frozen IMF*: The magnetic field’s long-range interactions induce correlations among particles, turning the system away from thermal equilibrium (e.g., Livadiotis & McComas 2014b), i.e., the kappa index decreases. The exact functional relationship between  $B$  and  $\kappa$  is not known, but qualitatively, we expect an inverse correspondence (negative correlation): the larger the magnetic field, the more intense the induced particle correlations, and the lower the kappa index; thus,  $B$  is negatively correlated with  $\kappa$ . While the magnetic energy further correlates the particles, the thermal energy, which is a measure of collisions, disorders the particles and destroys their correlations and thus competes with the magnetic energy, leading to a positive correlation between the values of  $T$  and  $\kappa$ . Then, the densities of magnetic and thermal energy have an opposite effect on the kappa index, that is, negative versus positive correlation, respectively. The competition between magnetic and thermal pressure can be represented by the plasma beta  $\beta$  (the ratio of thermal over magnetic pressure). As  $\beta$  increases, the magnetic over thermal pressure decreases, and thus, long-range interactions due to the magnetic field become weaker and the kappa index increases. Hence,  $\beta$  is *positively correlated with  $\kappa$* .

(iii) *Temperature fluctuations*: This mechanism is widely known (e.g., Beck & Cohen 2003; Touchette 2004; Vignat et al. 2005; Rajagopal 2006; Schwadron et al. 2010; Livadiotis et al. 2016) and is produced as a superposition of two statistics. Complex driven nonequilibrium systems, such as the solar wind, often exhibit dynamics that is a superposition of several dynamics on different timescales. For particles in a turbulent solar wind flow, the environmental conditions exhibit temperature fluctuations on a large spatiotemporal scale compared to local relaxation times. There is a relatively fast dynamics, given by the local particle distributions and their statistical mechanics, and also a slow one, given

by a spatiotemporally inhomogeneous parameter that varies globally with the environment. The two effects produce a superposition of two statistics, called “superstatistics” (named by Beck & Cohen 2003). According to the concept of superstatistics, local fluctuations of temperature shift the system into stationary states described by kappa distributions. The deviation from thermal equilibrium (measured by  $1/\kappa_0$ ) is proportional to the variation of the temperature fluctuations (standardized by the average temperature), so that  $1/\kappa_0 \sim \text{Var}(T)/T^2$  or  $\kappa_0 \sim T^2/\text{Var}(T)$ . Hence, the stabilized kappa index is given by

$$\kappa \cong A + B \cdot (\bar{T}/\delta T)^2 = A + B \cdot \delta T_r^{-2}, \quad (1)$$

where  $A$  and  $B$  are dimensionless constants related to the degrees of freedom. We observe that  $\kappa$  is negatively correlated with the variation of temperature fluctuations,  $\delta T^2$ .

Note that, while there are several known mechanisms that can generate kappa distributions and be applied to solar wind plasma near  $\sim 1$  au, they predict particular kappa indices; for example,  $\kappa \sim 2.4$  for the mechanism of weak turbulence (e.g., Yoon et al. 2012; Yoon 2014; Sunjung et al. 2015; and Chapter 8 in Livadiotis 2017), or  $\kappa \sim 1.5$  (approaching anti-equilibrium) (e.g., Fisk & Gloeckler 2014 and Chapter 15 in Livadiotis 2017). Most of these examples utilize the physical phenomena underlined by the discussed three plasma conditions.

The analysis presented in the next sections examines the characteristic relationships between the involved parameters ( $\kappa$ ,  $N_D$ ,  $\beta$ ,  $\delta T^2$ ), and detects the scales where each of the developed plasma conditions for generating kappa distributions exists and prevails.

### 3. Analysis of Kappa Indices

#### 3.1. Data Sets

We use  $\sim 92$  s solar wind plasma moments (speed  $V_{sw}$ , density  $n$ , and temperature  $T$  or thermal speed  $V_{th} = \sqrt{k_B T/m_i}$ ) (Ogilvie et al. 1995) and simultaneous measurements of IMF (Lepping et al. 1995), measured, respectively, from SWE and MAG onboard *Wind* spacecraft during the year 1995 (i.e.,  $\sim 336,800$  data samples; see Figures 2 and 3). (All datasets are publicly accessible at the mission database <https://wind.nasa.gov/data.php>, or at the OMNIWeb-Plus database, which includes the solar wind phase only, [https://omniweb.gsfc.nasa.gov/ftpbrowser/wind\\_swe\\_2m.html](https://omniweb.gsfc.nasa.gov/ftpbrowser/wind_swe_2m.html), where the solar wind and magnetospheric data were separated following King & Papitashvili 2005.) This time period occurred during the declining phase of solar activity cycle 23, and was characterized by corotating interaction regions that are apparent in increases in the solar wind density and magnetic field magnitude that precede

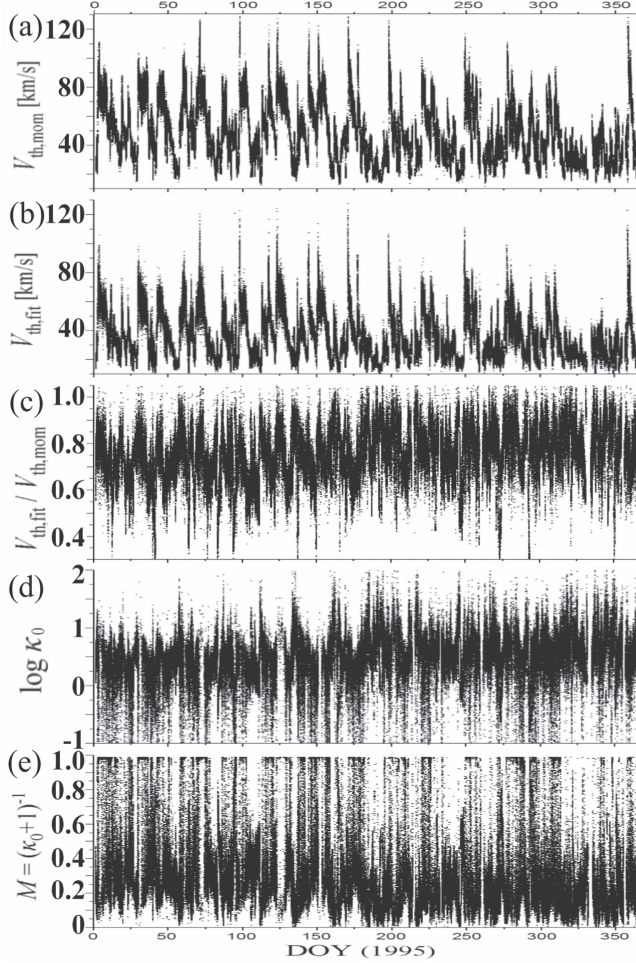


**Figure 3.** Measurements of bulk solar wind plasma parameters used for the kappa index estimation: thermal speeds, derived from (a) statistical moments,  $V_{\text{th},\text{mom}}$ , and (b) Maxwellian fitting of the core,  $V_{\text{th},\text{fit}}$ ; (c) their ratio  $V_{\text{th},\text{fit}}/V_{\text{th},\text{mom}}$ ; (d) the kappa index  $\kappa$ , estimated using (c) and Equation (3); (e) measure  $M = 1/(\kappa - 1/2)$ .

the arrival of the high speed streams at 1 au (e.g., Jian et al. 2006a, 2006b, 2009).

### 3.2. Method

There are two basic analytical/statistical methods that can be used to estimate the kappa indices from *Wind* data sets: (1) by fitting the solar wind 3D ion plasma distributions and (2) by analyzing the solar wind plasma moments. The data sets of distributions have resolution  $\sim 3$  s, i.e.,  $>30$  times higher than the  $\sim 92$  s resolution of the bulk solar wind data sets. Thus, two kappa index time series of different resolution ( $\sim 3$  s and  $\sim 92$  s) may be produced, which can be compared by smoothing and syncing the  $\sim 3$  s resolution to the  $\sim 92$  s resolution time series, and finally, derive the weighted mean of the two  $\sim 92$  s resolution time series. The first method of fitting has been applied numerous times in space plasma data analyses (e.g., see Pierrard et al. 1999). In this paper, we focus on the second method, which is explained and demonstrated below, in detail.

We estimate the kappa index by applying a technique that uses the high time-resolution data of bulk solar wind plasma properties, as shown in Figures 2 and 3. We use the thermal speeds (i)  $V_{\text{th},\text{fit}}$ , derived from the Maxwellian fitting of the core, and (ii)  $V_{\text{th},\text{mom}}$ , derived from the statistical moments. We note

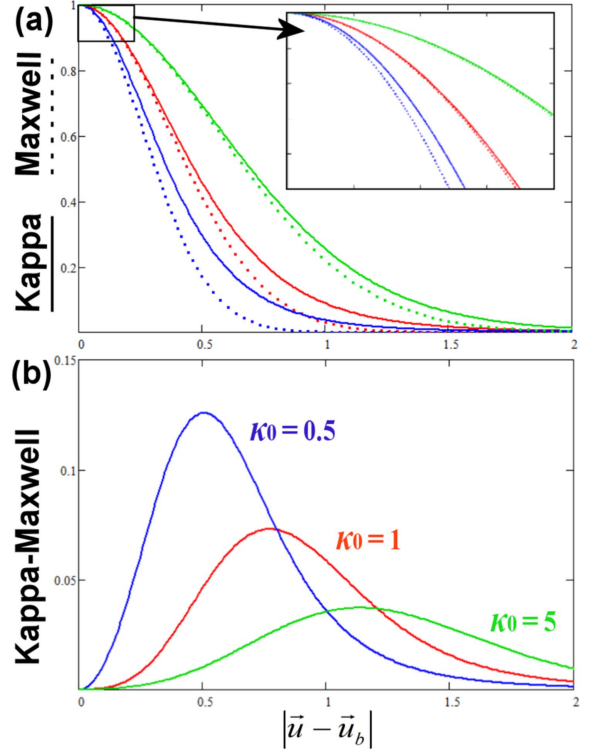


**Figure 4.** (a) Kappa (solid line) and Maxwell (dot line) functions are fitted to the core of a kappa distribution, which is normalized so that the maximum (at  $\varepsilon = 0$ ) to be set equal to 1, and for kappa indices  $\kappa_0 = 0.5$  (green),  $\kappa_0 = 1$  (red), and  $\kappa_0 = 5$  (blue). The kappa function is parametrized with temperature  $T$ , set to be  $\sqrt{2k_B T/m} = 1$ . The Maxwell function is parametrized with  $T_{\text{fit}}$ , set to be  $T_{\text{fit}} \equiv g(\kappa) \cdot T$ , according to Equation 2(b). (b) The algebraic difference between the kappa and Maxwell functions in (a), plotted for the same kappa indices.

that (i) by fitting a Maxwellian to the core of the observed distribution, the variance of the Maxwellian is used to compute the temperature and thermal speed, and (ii) as in most spacecraft data implementations, the temperature is derived as one-third of the trace of the pressure tensor in the bulk flow rest frame divided by the number density of that species; the corresponding thermal speed is then computed from this temperature estimation,  $V_{\text{th},\text{fit}} = \sqrt{k_B T_{\text{fit}}/m_i}$  and  $V_{\text{th},\text{mom}} = \sqrt{k_B T_{\text{mom}}/m_i}$ .

The method is based on the work of Nicolaou & Livadiotis (2016) that examines the possible misestimation of temperature when observations from a kappa distributed plasma are analyzed as a Maxwellian. According to this, by fitting the core of a kappa distribution  $f(\varepsilon)$  with a Maxwellian function, we misestimate the actual value of the temperature, but there is a relationship between the fitting temperature  $T_{\text{fit}}$  and the actual temperature  $T$ : the kappa distribution of the kinetic energy,  $\varepsilon(\mathbf{u}) = \frac{1}{2}m(\mathbf{u} - \mathbf{u}_b)^2$ , can be approximated for small values of energy to a Maxwell distribution, i.e.,

$$f(\varepsilon) \propto \left[ 1 + \frac{\varepsilon}{(\kappa - \frac{3}{2})k_B T} \right]^{-\kappa-1} \approx e^{-\frac{\varepsilon}{k_B T_{\text{fit}}}},$$

for  $\varepsilon \ll (\kappa - \frac{3}{2})k_B T$ , with (2a)

$$T_{\text{fit}} \equiv g(\kappa) \cdot T, \quad g(\kappa) \equiv \frac{\kappa - \frac{3}{2}}{\kappa + 1} = \frac{\kappa_0}{\kappa_0 + \frac{5}{2}}. \quad (2b)$$

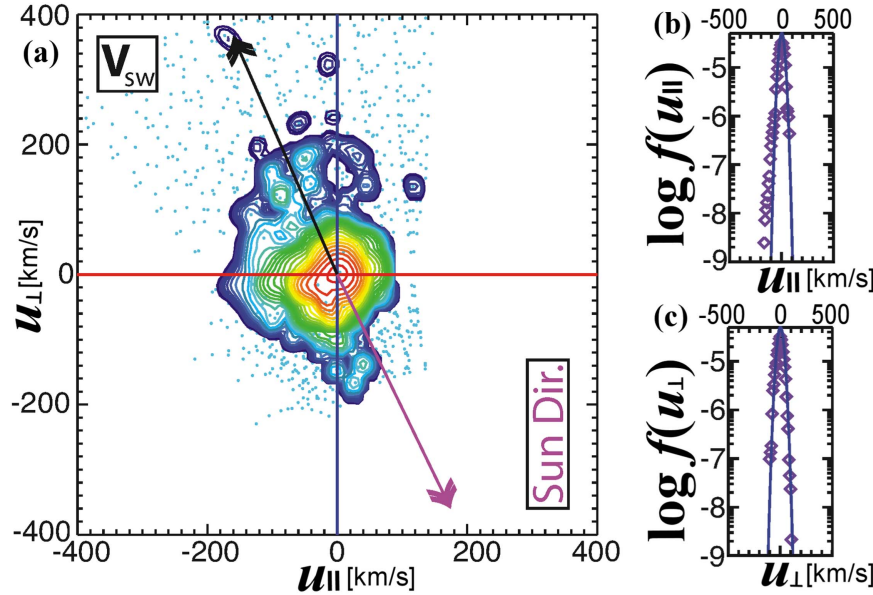


**Figure 5.** (a) 3D ion distribution of velocity analyzed to components  $\{u_{\parallel}, u_{\perp}\}$  parallel and perpendicular to the magnetic field, respectively. (b) Parallel and (c) perpendicular cuts of the 3D distribution. (DOY: 2000-04-06/16:31:19-22,  $\mathbf{V}_{\text{SW}} = \{-388.81, -12.33, -22.08\}$  [GSE,  $\text{km s}^{-1}$ ],  $\mathbf{B} = \{+2.77, -5.67, -0.67\}$  [GSE, nT]). (Data recorded from *Wind*/3DP, Pesa Low Burst, publicly accessible at <http://sprg.ssl.berkeley.edu/wind3dp/data/wi/3dp/lz/2000/>; see discussion of plot procedures in Wilson et al. 2010, 2014a, 2014b.)

(In our example, the bulk velocity is the solar wind velocity,  $\mathbf{u}_b = \mathbf{V}_{\text{SW}}$ .) Figure 4 shows three examples of a kappa distribution, where its core is fitted by a Maxwellian distribution with the parameter  $T_{\text{fit}}$  given by Equation 2(b).

The actual temperature can be calculated by using the statistical moments of the velocity distribution,  $T \sim T_{\text{mom}}$ . (Note that the contribution of other ion populations, such as, alpha and pickup ions, can be ignored, as it is shown in Appendix B.) Then, Equation 2(b) is written in terms of thermal speeds,  $V_{\text{th,fit}} \equiv \sqrt{g(\kappa)} \cdot V_{\text{th,mom}}$ . Therefore, the kappa index can be related to the ratio of the thermal speeds, as follows:

$$T_{\text{fit}} \equiv g(\kappa) \cdot T_{\text{mom}} \text{ and } V_{\text{th,fit}} \equiv \sqrt{g(\kappa)} \cdot V_{\text{th,mom}} \text{ with } g(\kappa) \equiv \frac{\kappa - \frac{3}{2}}{\kappa + 1} \Rightarrow \kappa = \frac{3}{2} + \frac{5}{2} \cdot (R^{-2} - 1)^{-1}, R \equiv \frac{V_{\text{th,fit}}}{V_{\text{th,mom}}} \quad (3)$$

Further, below, we demonstrate both the methods of kappa index estimation in a single example.

The selected example of ion velocity distribution is taken from the 3DP instrument onboard *Wind* for DOY 2000-04-06/16:31:19-16:31:22 and plotted in Figure 5 (the distributions are publicly accessible in <http://sprg.ssl.berkeley.edu/wind3dp/data/wi/3dp/lz/>; see Lin et al. 1995; Wilson et al. 2010, 2014a, 2014b). Panel (a) plots the 3D velocity anisotropic distribution, where the velocity is analyzed to components parallel  $u_{\parallel}$  and perpendicular  $u_{\perp}$  to the magnetic field  $\mathbf{B}$ . (The perpendicular cut is a 2D distribution; this is considered symmetric—no significant azimuth dependence, thus, only a 1D distribution is plotted, i.e., against the magnitude of the vector  $\mathbf{u}_{\perp} = (\mathbf{B} \times \mathbf{V}_{\text{sw}}) \times \mathbf{B}$ .) Panels (b) and (c) show the parallel and perpendicular cuts of the distribution, respectively. We choose the parallel cut to demonstrate the estimation of the kappa index, as shown in Figure 6.

In Figure 7(a), we fit the core (red) and halo (blue) ion distribution. In Figure 7(b), we focus on the core distribution, where we fit a Maxwell (light blue) and a kappa (purple) function. The fitting procedure involves minimizing the total square deviations between the modeled (Maxwell or kappa) function and the observed distribution, in order to derive the optimal values of the fitting parameters (e.g., Livadiotis 2007): The Maxwell distribution is simply parameterized by the thermal speed, for which the fitting gives  $V_{\text{th,fit}} \approx 31.5 \text{ km s}^{-1}$  (Figure 7(c), upper panel). The kappa distribution is parameterized by both the thermal speed and the kappa index; however, the thermal speed is not optimized but set to be equal to the moment value, which is estimated to be  $V_{\text{th,mom}} \approx 38.5 \text{ km s}^{-1}$ ; then, the fitting gives the optimal kappa index  $\kappa_0 \equiv \kappa - \frac{3}{2} \approx 5$  or  $\kappa \approx 6.5$  (Figure 7(c), lower panel).

Aside from fitting the solar wind plasma distribution with kappa functions, we also estimate the kappa index using the technique indicated in Equation (3). According to this technique, the kappa index is estimated using the ratio of the two thermal speeds, the one derived from the Maxwellian fitting of the core over the other derived from the statistical moments,  $R \equiv V_{\text{th,fit}}/V_{\text{th,mom}}$ . The ratio is  $R \approx 0.82$ , leading again to  $\kappa_0 \equiv \kappa - \frac{3}{2} \approx 5$  or  $\kappa \approx 6.5$  (Figure 7(d)). Both the methods of finding the kappa index from (1) fitting the solar wind plasma distributions and (2) using the solar wind plasma parameters and Equation (3), lead to the same value of kappa index. However, the fitting in the first method provides kappa indices with high time-resolution,  $\sim 3$  s, while the technique in the second method provides kappa indices with lower resolution,  $\sim 92$  s. The fact that the two methods end up with the same result, indicates that the kappa index may be less variant in a scale of  $\sim 1$  minute, compared to larger periods of time, where exhibits significant variability (e.g., see the time series of kappa indices, plotted in Figure 3, derived from the technique described above applied to the examined sample of the year 1995).

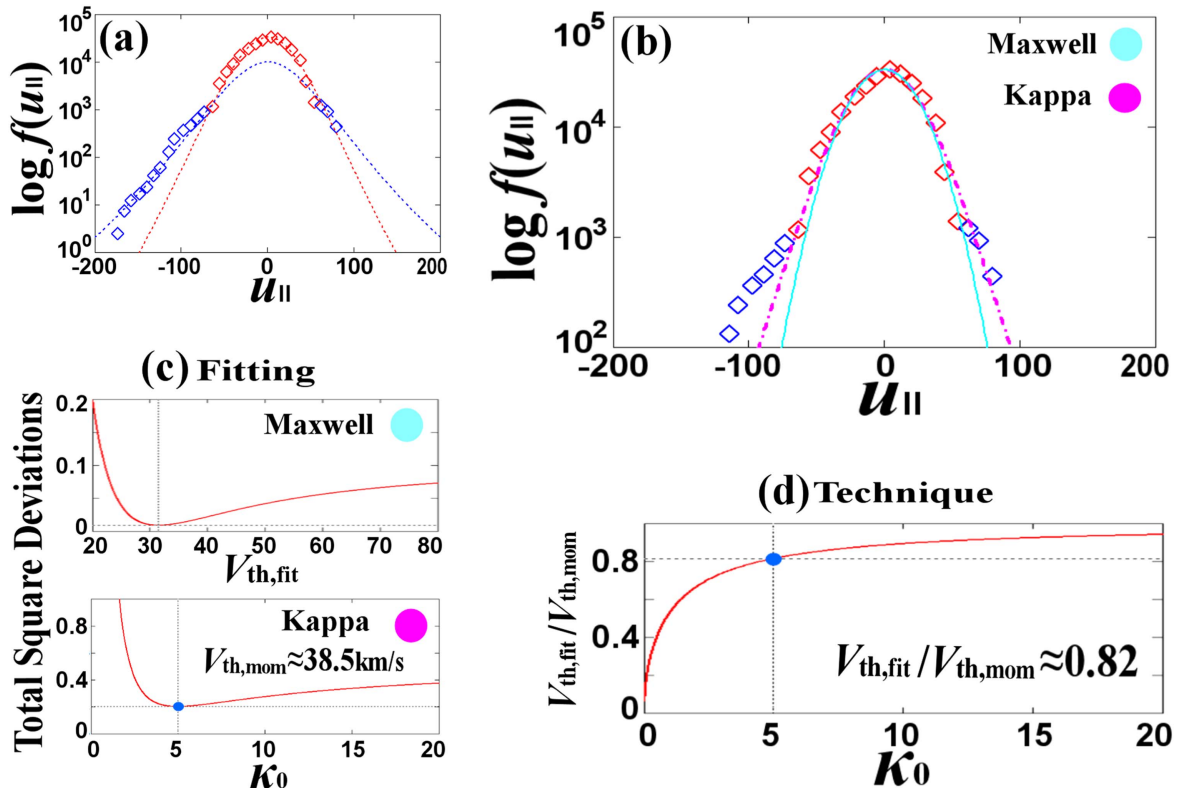


**Figure 6.** (a) Fitting of kappa distributions to the core (red) and halo (blue) ion populations. (b) Comparison between fitting of the core with a Maxwell (light blue) and a kappa (purple) function. (c) Fitting a Maxwellian distribution optimizes thermal speed to  $V_{\text{th,fit}} \approx 31.5 \text{ km s}^{-1}$ . Fitting a kappa distribution, for the given  $V_{\text{th,mom}} \approx 38.5 \text{ km s}^{-1}$  (calculated using the red points in panel (b)), optimizes the kappa index to  $\kappa_0 \approx 5$  (or  $\kappa \approx 6.5$ ). (d) The ratio of the two thermal speeds gives the same kappa index,  $\kappa_0 \approx 5$  (blue dot).

#### 4. Results

Our goal is to detect and study the plasma conditions for the generation of kappa distributions and the coupling of energy between solar wind plasma and IMF and for different types of solar wind modes. In order to address this goal, we (1) determine the kappa distributions (kappa indices) that characterize the solar wind plasma at 1 au; (2) detect relationships between the bulk solar wind properties (speed, temperature, density, etc.), the IMF, and the derived kappa indices; and (3) identify the mechanisms responsible for generating kappa distributions by distinguishing the kappa-plasma-magnetic field relationships.

##### 4.1. Estimated Kappa Indices

Figure 7 presents the steps to apply the technique for deriving the kappa indices from the ratio of thermal speeds, as shown in Equation (3) and demonstrated in Figure 6: For a certain time interval, we first plot the thermal speed  $V_{\text{th,fit}}$ , derived from a Maxwellian fitting of the core, against the thermal speed  $V_{\text{th,mom}}$ , derived from the statistical moments (Figure 7(a)). We observe that  $V_{\text{th,fit}} < V_{\text{th,mom}}$  for the majority of the data points, which verifies Equation (3) and thus it is a good indicator to proceed with the technique to derive kappa indices; otherwise, a filter can be applied to include only the cases of good fitting (for this, both chi-square and standard error of the fitted thermal speeds are provided by *Wind* data, though, they are not shown in Figures 2 and 3). Second, we plot the mean and standard errors for the thermal speeds  $V_{\text{th,fit}}$  and  $V_{\text{th,mom}}$ , estimated in each  $V_{\text{sw}}$ -bin (Figure 7(b)), as well as their normalized 2D histograms against the solar wind speed

$V_{\text{sw}}$  (Figures 7(c)–(e)). Finally, we plot the kappa indices derived from Equation (3) (Figure 7(f)).

Figure 8(a) displays the occurrence frequency of  $V_{\text{sw}}$  observed during the 1 year period of 1995, shown in Figure 2(a), while Figure 8(b) shows the 2D occurrence frequency of the logarithm of kappa index from Figure 3(d) versus  $V_{\text{sw}}$ . Figure 8(a) demonstrates the nearly bimodal nature of  $V_{\text{sw}}$  in these observations, with respective averages  $\sim 400 \text{ km s}^{-1}$  and  $\sim 620 \text{ km s}^{-1}$ ; however, the peak of the slow wind is modest compared to the fast solar wind. For this one year period, the separation between the slow and fast wind is  $\sim 550 \text{ km s}^{-1}$ . Given the sampling distribution of the different solar wind speeds, it is not surprising that the 2D histogram of the kappa indices versus  $V_{\text{sw}}$  in Figure 8(b) also shows two maxima and a minimum, corresponding to the peaks seen in Figure 8(a). We therefore normalize the 2D histograms to investigate the actual relationship between  $V_{\text{sw}}$  and the logarithm of kappa index,  $\log(\kappa - 3/2)$ . Figure 8(c) shows the 2D histogram normalized by the 1D histogram of  $V_{\text{sw}}$ , which clearly demonstrates that the distribution of kappa indices during this one year interval is mostly independent of the solar wind speed, at least for speed less than  $\sim 620 \text{ km s}^{-1}$ ; this independence of kappa indices with respect to  $V_{\text{sw}}$  is also shown in Figure 8(d). This figure shows the average values of the logarithm of  $\kappa_0 \equiv \kappa - 3/2$ , estimated for each of the  $V_{\text{sw}}$ -bins. The 1D histogram in Figure 8(e) indicates that the peak or mean value of  $\log(\kappa - 3/2)$  from all the bins is  $\approx 0.45 \pm 0.10$ , which corresponds to  $\kappa_0 \approx 2.8 \pm 0.7$  or  $\kappa \approx 4.3 \pm 0.7$ , and is consistent previously published estimations of kappa index in the solar wind (Livadiotis 2015a, and references therein).

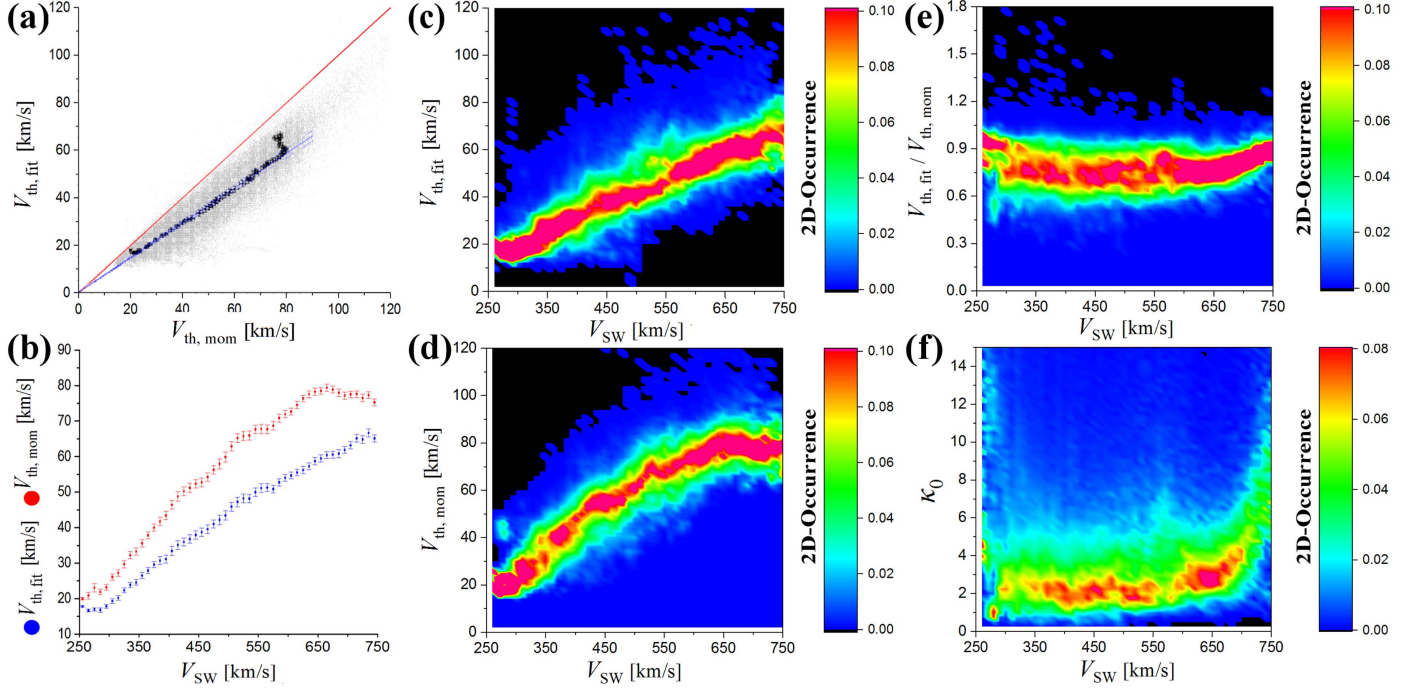


**Figure 7.** Derivation of kappa indices using Equation 2(b): (a) Plot of thermal speeds,  $V_{\text{th,fit}}$  vs.  $V_{\text{th,mom}}$  (gray); we observe that all points are below the (red) diagonal, i.e.,  $V_{\text{th,fit}} < V_{\text{th,mom}}$ , verifying Equations (3) that  $g(\kappa) < 1$ . (b) Means and standard errors for the thermal speeds, estimated in each  $V_{\text{SW}}$ -bin. Their mean values are also co-plotted in (a), where we observe that they are linearly distributed, indicating the most frequent kappa index  $\kappa_0 \approx 2.8$  or  $\kappa \approx 4.3$ . (c)–(f) 2D histograms of  $V_{\text{th,fit}}$ ,  $V_{\text{th,mom}}$ , the ratio  $V_{\text{th,fit}}/V_{\text{th,mom}}$ , and the kappa indices ( $\kappa_0 = \kappa - 3/2$ ), respectively (all plotted against  $V_{\text{sw}}$ ). All 2D histograms are normalized by the 1D histogram of  $V_{\text{sw}}$  distribution (shown in Figure 8(a)).

Finally, we remark that the mode of the histogram of kappa indices, plotted in Figure 7(f), that is, the most frequent value of kappa indices, is located at  $\kappa_0 \sim 2.2$ . However, the respective mode of the histogram of the logarithm of kappa indices, plotted in Figure 8(c), is located at  $\log \kappa_0 \sim 0.45$ , corresponding to  $\kappa_0 \sim 2.8$ . This must not be surprising: if  $P_X(x)$  is the histogram (distribution density) of the values of a variable  $x$ , having a mode at  $x_*$ ,  $P'_X(x = x_*) = 0$ , then the histogram  $P_Y(y)$  of the values of some variable  $y = f(x)$  may have a mode at  $y_*$ ,  $P'_Y(y = y_*) = 0$ , where  $y_*$  is, in general, different than  $f(x_*)$ . The equality  $y_* = f(x_*)$  could have happened if the two histograms were both symmetric. In our case, the histograms of  $\kappa_0$  and  $\log \kappa_0$  are asymmetric and symmetric, respectively. When the histogram is symmetric, then the mean value coincides with the most frequent one (e.g., see Livadiotis 2012). The appropriate variable to be involved in any statistical analyses is the one described by a symmetric distribution, such as, the histogram of  $\log \kappa_0$  in Figure 8(c). (We may also note that solar wind moments are typically described by a log-normal distribution, namely, the logarithm of the moments is described by normal distributions.)

#### 4.2. Detected Relationships

Having derived the time series of kappa indices, we can construct the 2D histograms of these indices with the solar wind proton temperature, density, and magnetic field data sets (shown in Figure 2). In Figure 9, we plot the 1D histogram of the abscissa  $\log X$  and the raw (left) and normalized (right) 2D histograms of  $\log X$  and  $\log \kappa_0$ , where  $X$  represents (a) temperature, (b) density, and (c) magnetic field strength. As explained in the construction of Figure 8(c), the normalized 2D

histogram is derived using the 1D histogram of the abscissa. In panel (a), we observe that the kappa indices attain a small local maximum at  $\log \kappa_0 \sim 1.1$  for temperatures  $\log T \sim 0.5$  and a broader minimum at  $\log \kappa_0 \sim 0.4$  for higher temperatures  $\log T \sim 1.4$ , while the kappa index clearly increases with temperature for  $\log T > 1.6$ . In panel (b), the kappa index increases with density for  $\log n < 0.5$ , but is rather constant for larger densities. In panel (c), we observe that the kappa index remains roughly constant for very small or high magnetic field values but it increases for moderate values,  $0.5 < \log B < 0.9$ .

Further below we construct the 2D histograms of the logarithm of the kappa index,  $\log \kappa_0$ , against the logarithms of the Debye number,  $\log N_D$ , and the plasma beta,  $\log \beta$ . Figure 10(a) plots a normalized 2D histogram by binning the logarithm of kappa indices as ordinates, taken from Figure 3(d), and the logarithm of the Debye number  $N_D$  as abscissae. (Note that the Debye number depends also on the kappa index (Bryant 1996; Rubab & Murtaza 2006; Gougam & Tribeche 2011; Livadiotis & McComas 2014a), but the coupling parameter  $\Gamma$  does not, so that their relation should actually be given by the Debye number at thermal equilibrium,  $N_{D_\infty}$ , i.e.,  $\Gamma \cong 0.1 \cdot N_{D_\infty}^{-2/3}$ ; hereafter, we keep the symbol  $N_D$ , instead of  $N_{D_\infty}$ , for simplicity.) The Debye number is given by  $N_D = (4\pi/3)n \lambda_D^3$ , or  $N_D = 1.721 \times 10^9 \cdot (T/\text{[eV]})^{3/2} (n/\text{[m}^{-3}\text{]})^{-1/2}$ , with  $n/\text{[m}^{-3}\text{]}$  and  $T/\text{[eV]}$  taken from Figures 2(b) and (c), respectively. As in Figure 8(c), we normalize the raw 2D histograms by the corresponding 1D histogram of the abscissa, that is, the logarithm of Debye number in this instance. Figure 10(b) plots a similar normalized 2D histogram by binning again the logarithm of the kappa indices as ordinate, but against the logarithm of the plasma beta as abscissa, taken from Figure 2(e). In Figure 10(a), we observe that the most frequent kappa indices decrease as the

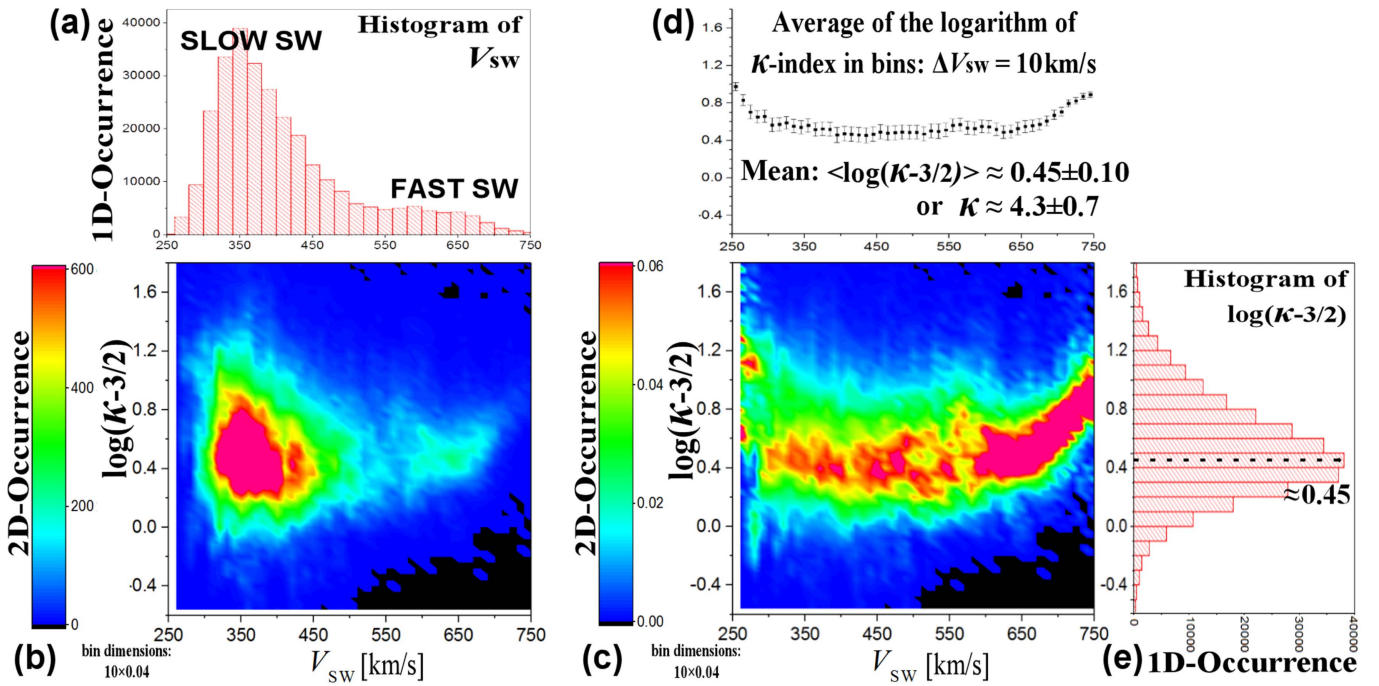


**Figure 8.** (a) 1D histogram (or occurrence frequency) of the solar wind speed  $V_{\text{SW}}$  observed during the one year interval (1995) shown in Figure 2(a). (b) 2D histogram of the logarithm of kappa indices ( $\log \kappa_0$  with  $\kappa_0 = \kappa - 3/2$ ; shown in Figure 3(d)) vs.  $V_{\text{SW}}$ . (c) 2D histogram from Figure 8(b) normalized by the  $V_{\text{SW}}$  distribution in Figure 8(a). (d) Means and standard errors for the kappa indices ( $\log \kappa_0$ ) in each  $V_{\text{SW}}$ -bin. (e) 1D histogram of all values of  $\log \kappa_0$ .

Debye number increases becoming roughly constant for  $\log N_D > 10.8$ . In panel (b) we observe that the kappa index increases with the plasma beta reaching a maximum at  $\log \kappa_0 \sim 0.7$  for  $\log \beta \sim -0.3$ ; then, the kappa index decreases becoming roughly constant for  $\log \beta > 0.6$ .

## 5. Discussion

Here, we discuss the identified plasma conditions for generating kappa distributions, and their effects and variations with solar wind features. We examine: (i) the solar wind modes; (ii) the possible dispersion of the fast magnetosonic waves and the efficiency of the transferred magnetosonic energy; and (iii) the polytropes, i.e., the connection between kappa and polytropic indices.

### 5.1. Identified Conditions for Generating Kappa Distributions

In Figure 11 we show the average behavior of the kappa index with respect to the Debye number and the plasma beta. Figure 11(a) plots the average values of the logarithm of  $\kappa_0 \equiv \kappa - \frac{3}{2}$ , estimated for each of the ( $\log N_D$ ) bins, (similar to Figure 8(e)). Figure 11(b) shows the average values of  $\log \kappa_0$ , estimated now for each of the ( $\log \beta$ ) bins. Figure 10(c) shows the relation (positive correlation, on average) between the logarithms of the plasma beta and the Debye number by plotting the average values of ( $\log \beta$ ) estimated for each of the ( $\log N_D$ ) bins.

We observe that the kappa index decreases as the Debye number increases in the interval from  $\log N_D \sim 9.5$  to  $\log N_D \sim 11$  (Figure 11(a)). The Debye number is positively correlated with the plasma beta  $\beta$  (Figure 11(c)), with the interval  $9.5 < \log N_D < 11$  corresponding to  $-0.1 < \log \beta < 0.1$ . Debye

numbers, smaller than  $N_D \sim 9.5$ , correspond to plasma beta values smaller than  $\log \beta \sim -0.1$ , that is, higher magnetic over thermal pressure, and thus, the magnetic field is more effective in binding and correlating particles. Indeed, in Figure 11(b), we observe that, for  $\log \beta < -0.1$ , the kappa index decreases as the plasma beta decreases or the ratio of the magnetic over thermal pressure increases. Moreover, at large scales, such as  $\log N_D > 11$  or  $\log \beta > 0.1$ , the kappa index is less sensitive. The analysis shown in Figure 12 reveals that at high temperatures, the temperature fluctuations constitute the primary mechanism for generating kappa distributions away from the thermal equilibrium.

We estimate the averages of temperature fluctuations as follows: using the bulk solar wind plasma temperature data, shown in Figure 2(c), we calculate the consecutive temperature deviations  $\Delta T_i = |T_{i+1} - T_i|$  between the  $i$ th and  $(i+1)$ th data points. For accurate estimation, we may apply several filters, such as to calculate  $\Delta T_i$  only for small relative error, e.g.,  $\delta \Delta T_i / \Delta T_i < 1/3$ , or when the  $i$ th and  $(i+1)$ th data points correspond to approximately equal Bernoulli integral (Livadiotis 2016), which reduces the possibility of acquiring an unphysical deviations because of streamline crossing (Kartalev et al. 2006; Nicolaou et al. 2014). Then the calculated temperature deviations are arranged in terms of increasing temperature, their mean values are estimated for each of the ( $\log T$ ) bins, and plotted in Figure 12(a); these constitute the representative values of the temperature fluctuations. In this panel, we observe that for temperatures less than the threshold given by  $\log(T_2/\text{[eV]}) \sim 1.6$ , the temperature fluctuations are proportional to temperature,  $\Delta T \propto T$ , while for higher temperatures,  $T > T_2$ , the temperature fluctuations are less sensitive to temperature,  $\Delta T \propto T^{3/4}$ . Given Equation (1), the proportionality  $\Delta T \propto T$  corresponds to constant kappa indices, while

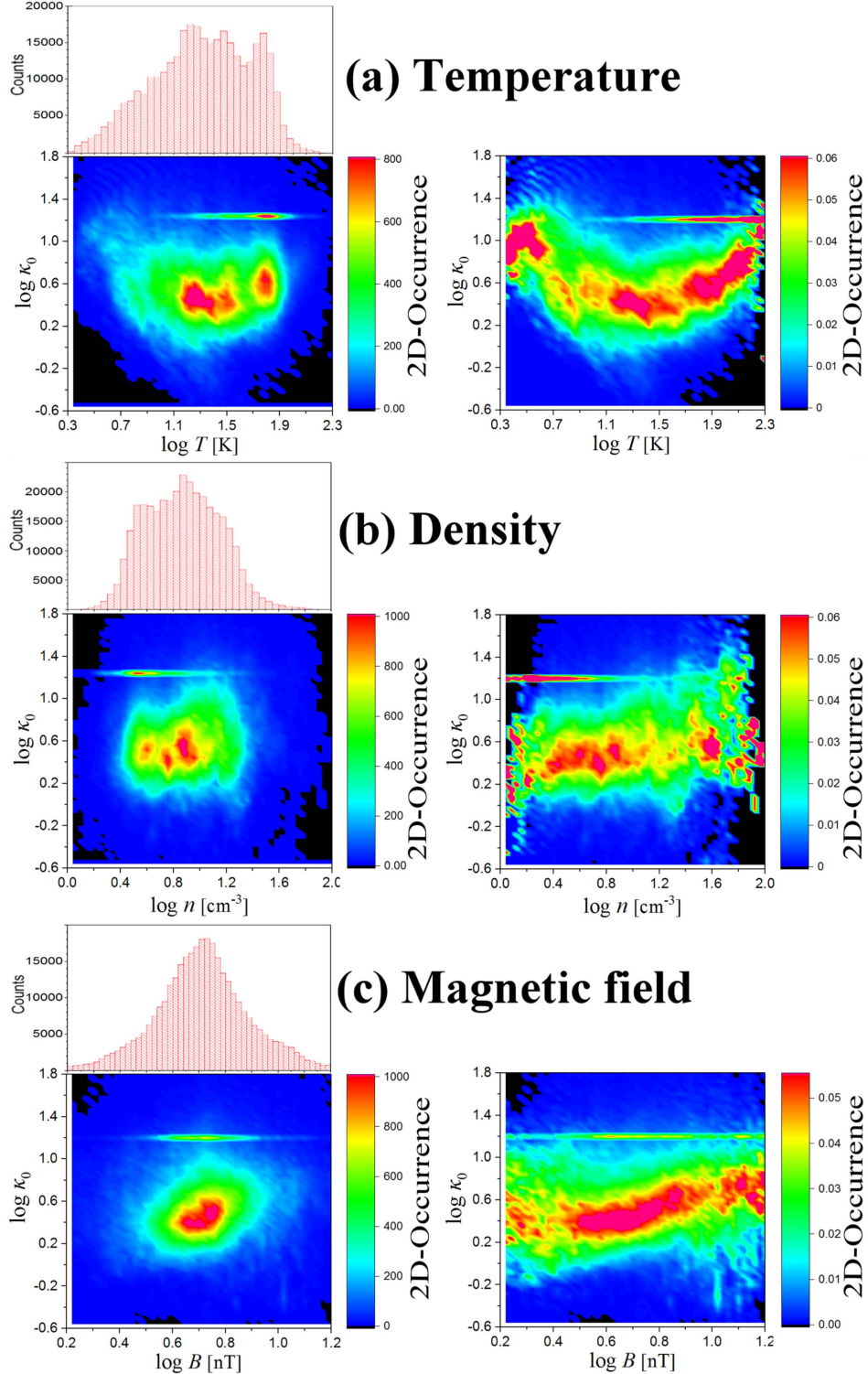


**Figure 9.** Plots of 1D histogram of the abscissa  $\log X$  and 2D histograms of  $\log X$  and  $\log \kappa_0$ , both raw (left) and normalized (right) for  $X$ : (a) temperature, (b) density, and (c) magnetic field strength. (We plotted the unfiltered raw data as shown in Figure 2.)

$\Delta T \propto T^{3/4}$  corresponds to kappa indices positively correlated to temperature,  $\kappa_0 \propto \sqrt{T}$ . This is confirmed in Figure 12(b) where the kappa index is plotted against the temperature.

The three identified solar wind plasma conditions of Debye shielding, frozen IMF, and temperature fluctuations prevail in different scales of solar wind plasma parameters and IMF:

1.  $\beta$  region: For small values of the plasma beta,  $\beta < \beta_1$  with  $\log \beta_1 \sim -0.1$ , there is higher magnetic over thermal pressure so that the magnetic field is more effective for generating correlations among particles, becoming the primary mechanism for generating kappa distributions (Figure 11(b)). The Debye number is also

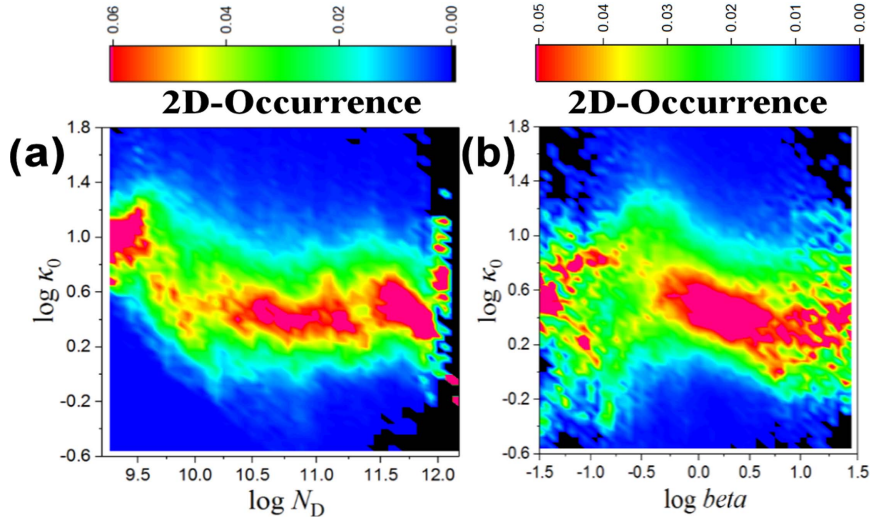


**Figure 10.** 2D histograms of the logarithm of kappa indices,  $\kappa_0 = \kappa - 3/2$  vs. (a) the logarithm of the Debye number,  $\log N_D$ , and (b) the logarithm of the plasma beta,  $\log \beta$ . (The data sets were filtered by using only points with small relative errors,  $<1/3$ , in all the used parameters.)

- small (Figures 11(a), (c)),  $N_D < N_{D1}$  with  $\log N_{D1} \sim 9.5$ , so that the Debye shielding is a less important mechanism.
2.  $N_D$  region: For larger values of the plasma beta,  $\beta_1 < \beta$ , the Debye number is also larger,  $N_{D1} < N_D$ , and eventually, the impact of the magnetic field is overridden by the Debye shielding (Figures 11(a), (b)) that induces correlations among particles within the Debye spheres.
  3.  $\delta T$  region: For even larger values of the Debye number,  $N_{D2} < N_D$  with  $\log N_{D2} \sim 11$ , the Debye shielding becomes less effective, while the correlation due to the magnetic field is even less important. In these high temperatures, one of the mechanisms responsible for generating kappa distributions is the temperature fluctuations (Figure 12).

## 5.2. Effects and Variations with Solar Wind Parameters

### 5.2.1. Slow versus Fast Solar Wind

Figures 7(f) and 8(c) show that the kappa index has different dependence on the solar wind speed for slow and fast modes. The slow mode is characterized by a quasi-constant kappa index, evaluated in Figure 8(e) as  $\log \kappa_0 \approx 0.45 \pm 0.10$  or  $\kappa \approx 4.3 \pm 0.7$ . The fast mode beyond  $\sim 620 \text{ km s}^{-1}$  exhibits kappa indices increasing with solar wind speed ( $\log \kappa_0$  linearly increasing with  $V_{\text{SW}}$ ).

According to Figures 11 and 12, the three plasma conditions may lead to an increasing kappa index if one (or more) of the parameters  $1/\beta$ ,  $N_D$ ,  $\delta T$ , decreases. Higher values of kappa indices can be generated for small values of  $1/\beta$  and  $N_D$  near the boundary values  $\beta \sim \beta_1$  and  $N_D \sim N_{D1}$  where the two conditions of the Debye shielding and frozen magnetic field are equally effective. Therefore, these two mechanisms are more likely for the fast mode solar wind that exhibits higher kappa indices.

### 5.2.2. Dispersion of Fast Magnetosonic Waves

Recently, it was shown that the transfer of energy between solar wind plasma particles and waves is governed by a new and unique relationship—the ratio between the magnetosonic energy  $E_{\text{ms}}$  over the primary plasma frequency  $\omega_{\text{pl}}$ , i.e.,  $E_{\text{ms}}/\omega_{\text{pl}} = \hbar_*$ , has a constant value  $\hbar_* \approx (1.19 \pm 0.05) \times 10^{-22} \text{ J s}$  (Livadiotis

2017, Chapter 5; see also: Livadiotis & McComas 2013b; Livadiotis 2015d). The variability of the ratio  $E_{\text{ms}}/\omega_{\text{pl}}$  from the expected constant value of  $\hbar_*$  was found to characterize the low latitudes solar wind in the inner heliosphere (Livadiotis & McComas 2014b; Livadiotis 2015d). This variability can be exploited to shed light to attenuation phenomena that characterize magnetosonic waves in solar wind, e.g., dispersion, damping, scattering, etc. For example, considering that dispersion is taken place, then, the quantum  $\hbar_* \omega_{\text{pl}}$  interprets the energy associated with the group magnetosonic speed while the observed variations interprets the energy associated with the phase magnetosonic speed, Livadiotis & Desai (2016) were able to derive the frequency–wavenumber relationship and other characteristics of the dispersion. Previous analyses showed that fast magnetosonic waves become dispersive (e.g., Roberts 1991; Nakariakov & Roberts 1995; Nakariakov et al. 1996; Roberts & Ulmschneider 1997; Pascoe et al. 2014; Shestov et al. 2015). Also, Murawski et al. (2001) analytically derived dispersion relations for fast magnetosonic waves propagating through plasma with a randomly structured magnetic field, while Narita et al. (2011) found observationally the dispersion relations of turbulent magnetic fluctuations in solar wind.

According to the dispersion relation derived by Livadiotis & Desai (2016), the ratio  $E_{\text{ms}}/\omega_{\text{pl}}$  transitions continuously from the slow to the fast solar wind, tending toward the coupling constant  $\hbar_*$ . Therefore, in contrast to the efficiently transferred magnetosonic energy in the fast solar wind, the lower efficiency of the slow solar wind can be caused by dispersion of fast magnetosonic waves. Figure 13 plots both the (a) kappa index  $\kappa_0$  and (b) the ratio between the magnetosonic energy over the plasma frequency,  $\log(E_{\text{ms}}/\omega_{\text{pl}})$ , against the solar wind speed  $V_{\text{SW}}$ .

We observe that both parameters, (a) the kappa index  $\kappa_0$  and (b) the ratio between the magnetosonic energy over the plasma frequency,  $\log(E_{\text{ms}}/\omega_{\text{pl}})$ , are positively correlated with the solar wind speed  $V_{\text{SW}}$ . Moreover, for  $V_{\text{SW}} > 620 \text{ km s}^{-1}$ , the kappa index increases more steeply, leading plasma particles closer to thermal equilibrium (Figure 13(a)). On the other hand, for  $V_{\text{SW}} > 620 \text{ km s}^{-1}$ , the ratio  $E_{\text{ms}}/\omega_{\text{pl}}$  approaches  $\hbar_*$  (Figure 13(b)).

We find that the most frequent values of the kappa indices can be described by the empirical relationships:

$$\log \kappa_0 \cong 0.4 + 0.001 \cdot \exp[+(V_{\text{SW}}/325)^2], \quad (4a)$$

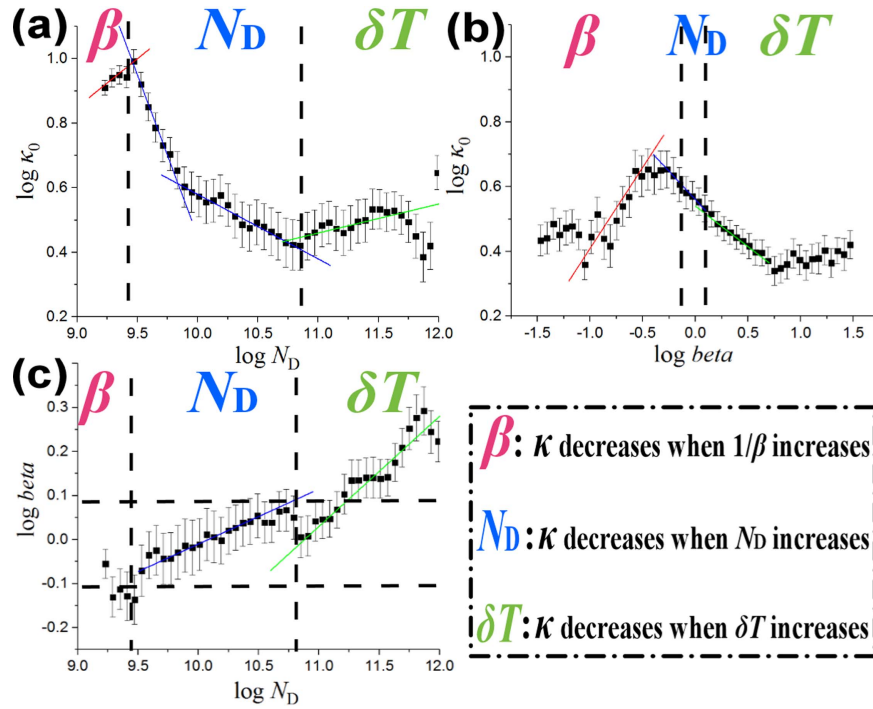


**Figure 11.** Means and standard errors of  $\log \kappa_0$ , estimated for each of the (a) ( $\log N_D$ ) bins and (b) ( $\log \beta$ ) bins. Also, in order to observe directly the relationship between the values of  $\log \beta$  and  $\log N_D$ , in panel (c) we plot the means and standard errors of the values of  $\log \beta$ , estimated for each of the ( $\log N_D$ ) bins. We observe three regions with significantly different coupling and dynamics. These are symbolized by  $\beta$ ,  $N_D$ ,  $\delta T$ , and reveal three different conditions that generate kappa distributions, that is, the effect of the frozen magnetic field binding, the Debye shielding, and the temperature fluctuations, respectively. (Panels (a) and (b) correspond to the normalized 2D histograms plotted in Figures 10(a) and (b), respectively. Note that the range of the variables  $\log \beta$  and  $\log N_D$  changes depending on which is the normalizing parameter.)

$$\log(E_{\text{ms}}/\omega_{\text{pl}}) \cong \log \hbar_* - 2.8 \cdot \exp[-(V_{\text{sw}}/325)^2]. \quad (4b)$$

Hence, canceling  $V_{\text{sw}}$ , we find

$$\ln[E_{\text{ms}}/(\hbar_* \omega_{\text{pl}})] \cong 0.015/(0.92 - \ln \kappa_0), \quad (4c)$$

that gives the dispersion relationship

$$\ln(V_{\text{ph}}/V_g) = d \ln \omega / d \ln k \cong 0.0075 / \ln(0.4 \kappa_0). \quad (4d)$$

Therefore, the dispersion is more effective for lower kappa indices (i.e., further from thermal equilibrium), thus it is involved in the two mechanisms of Debye shielding and magnetic field binding, which can generate higher kappa indices.

### 5.2.3. Connection between Kappa and Polytropic Indices

A polytropic relation connects the values of thermal variables (such as, density, temperature, thermal pressure, etc.) along a certain streamline of the plasma flow. A polytrope is a certain thermodynamic process characterized by such a relation. Typically, this is a power law between two thermodynamic variables, that is,  $P \propto n^\gamma$  or  $n \propto T^\nu$  with  $\nu \equiv 1/(\gamma - 1)$ .

Particle interactions assign specific relationships between the polytropic and kappa indices. Simple cases of potential energies can lead to a polytropic index given by  $1/(\gamma - 1) = \text{const.} - \kappa_0$ , where the involved constant is related to the involved potential degrees of freedom. There are three possible reasons for which the relationship between polytropic and kappa indices may be described by a more complicated function: (1) there are a variety of kappa distribution formulae describing the potential energy; (2) positional dependence of parameters characterizing kappa distributions; and (3) when the actual distribution function is given by a superposition of kappa

distributions; (for more details, see Livadiotis 2015c, 2017; Chapters 4 and 5). No significant effect is expected from these causes, thus the relationship should be still characterized by a positive correlation between polytropic and kappa indices. This is verified in Figure 14, where we plot (a) the logarithm of kappa indices,  $\log \kappa_0$ , and (b) the polytropic indices,  $\gamma$ , both against the solar wind speed.

## 6. Conclusions

The paper identified and studied three plasma conditions interwoven with the generation of kappa distributions in solar wind near 1 au. By analyzing the solar wind plasma properties (speed, density, temperature or thermal speed, and kappa index) and the simultaneous measurements of IMF, taken from publicly accessible *Wind* observations during the year 1995, we determined the characteristic relationships between these parameters that indicate the three detected plasma conditions.

The identified three plasma conditions are the following: (i) Debye shielding, (ii) frozen IMF, and (iii) temperature fluctuations (Table 1). The analysis detected the characteristic relationship of each plasma condition (that is, a correspondence between the kappa index and other key parameters); these relationships are, respectively: (i) the Debye number,  $N_D$ , is negatively correlated with the kappa index  $\kappa$ , (ii) the plasma beta,  $\beta$ , is positively correlated with  $\kappa$ , and (iii) the variation of temperature fluctuations,  $\delta T^2$ , is negatively correlated with  $\kappa$ . Each of these three conditions prevails in different scales of solar wind plasma properties and IMF.

The estimation of the kappa indices performs an important role in the presented analysis. These are derived from a technique (Nicolaou & Livadiotis 2016) that uses the bulk solar

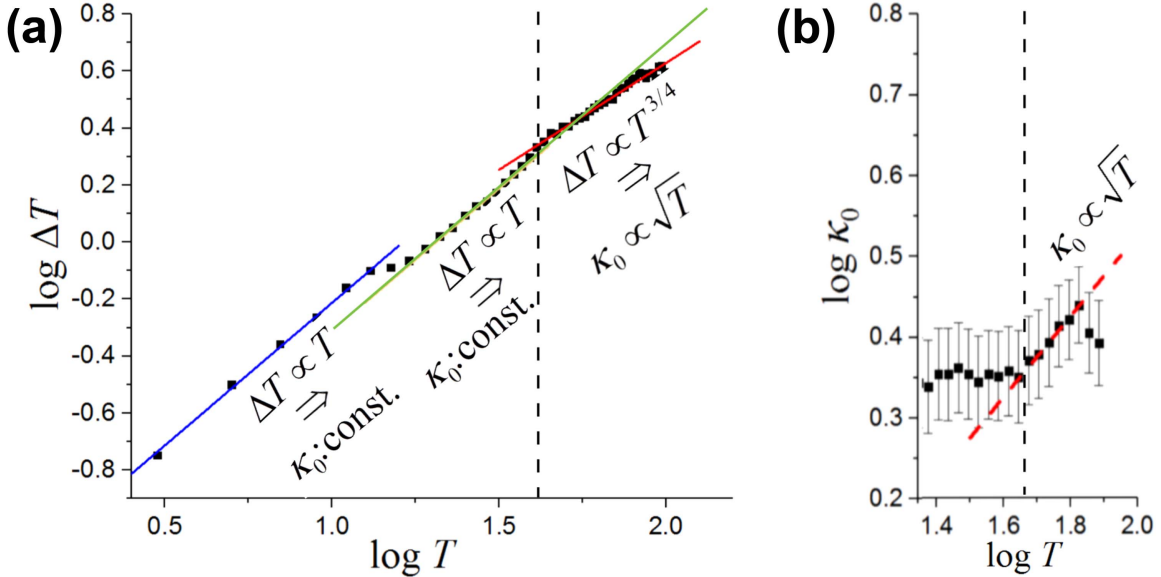


**Figure 12.** (a) Average temperature deviations  $\Delta T$ , derived from consecutive data points of Figure 2(c) arranged with increasing  $T$ , with their mean values estimated and plotted for each of the  $(\log T)$  bins. (b) Plot of the mean values and standard errors of  $\log \kappa_0$ , estimated for each of the  $(\log T)$  bins for  $\log T > 1.3$ . The detected power law between  $\Delta T$  and  $T$  corresponds to a certain relationship between  $\kappa$  and  $T$ , that is,  $\kappa_0 \sim \text{constant}$  for lower and  $\kappa_0 \propto \sqrt{T}$  for higher temperatures. (Temperature units: eV.)

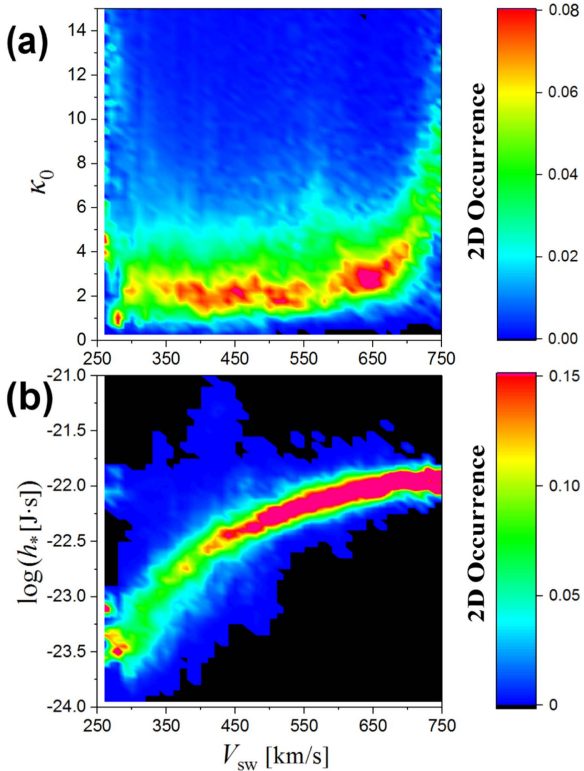


**Figure 13.** Normalized 2D histograms of (a) the kappa indices ( $\kappa_0 = \kappa - 3/2$ ) and (b) the ratio of the magnetosonic energy over the plasma frequency (on semi-log scale), which tends to the coupling constant  $\log(h_*/[\text{J} \cdot \text{s}]) \approx -22$  for large solar wind speeds (e.g., see Livadiotis & Desai 2016).

wind plasma parameters, that is, basically, the two thermal speeds, the one derived from a Maxwellian fitting and the other derived from the statistical moments (*Wind* data sets provide both thermal speeds together with errors and chi-square values that can be used for filtering the derived kappa indices). It was shown that:

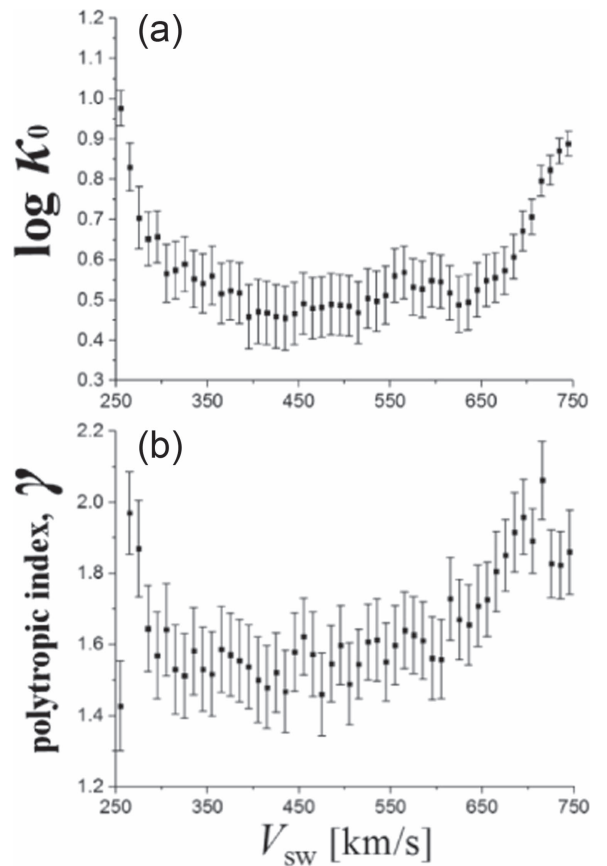


**Figure 14.** Plots of the mean values and standard errors of (a)  $\log \kappa_0$  and (b)  $\gamma$ , estimated for each of the  $V_{sw}$ -bins. (The polytropic indices have been derived using the method of Livadiotis & Desai (2016), and moving averages of five consecutive values of density and temperature; c.f. Figure 3 of that paper.)

- (1) The kappa indices have different dependence on the solar wind speed for slow and fast modes. Slow mode is characterized by a quasi-constant kappa index, i.e.,  $\log$

**Table 2**  
Error Estimation in Derived Quantities

X	$\delta X$
Kappa index $\kappa$ , via the technique in Equation (3) (Section 3.1); $\kappa = \frac{3}{2} + \frac{5}{2} \cdot (R^{-2} - 1)^{-1}$	$\delta\kappa = 5R^2(1 - R^2)^{-2}\delta\ln R$ , with $\delta\ln R = \sqrt{(\delta V_{\text{th,fit}}/V_{\text{th,fit}})^2 + 0.0016}$
Temperature fluctuation ( $\delta T$ ) (Section 3.2) $\Delta T_i =  T_{i+1} - T_i $	$\delta\Delta T_i = \sqrt{T_{i+1}^2 + T_i^2} \times 8\%$
Plasma beta, $\beta$ (Figure 2(e))	$\delta\log\beta \approx 0.04$
Units	$V_{\text{SW}}$ , $V_{\text{th}}$ in $[\text{km s}^{-1}]$ , $B$ in $[\text{nT}]$ , $n$ in $[\text{cm}^{-3}]$ , $T$ in $[\text{eV}]$ , Dimensionless: $\beta$ , $N_D$

$\kappa_0 \approx 0.45 \pm 0.10$  or  $\kappa \approx 4.3 \pm 0.7$ . Fast mode exhibits kappa indices that increase with the solar wind speed ( $\log \kappa_0$  linearly increases with  $V_{\text{SW}}$ , for  $V_{\text{SW}} > 620 \text{ km s}^{-1}$ ). The two conditions of Debye shielding and frozen magnetic field are more likely at the fast mode solar wind that exhibits higher kappa indices.

- (2) The kappa indices were found to be positively correlated with the values of the ratio of the magnetosonic energy over the plasma frequency,  $E_{\text{ms}}/\omega_{\text{pl}}$ , which tend to the coupling constant  $\hbar_* \approx (1.19 \pm 0.05) \times 10^{-22} \text{ J s}$  for  $V_{\text{SW}} > 620 \text{ km s}^{-1}$ . The dispersion is more effective for lower kappa indices (i.e., further from thermal equilibrium), and in this case, the two plasma conditions of Debye shielding and frozen magnetic field, which can generate larger kappa indices, are more likely to be involved.
- (3) The kappa and polytropic indices are also positively correlated. Particle interactions assign specific relations between the polytropic and kappa indices. Studying these relations we may be able to characterize the underlying interactions and dynamics that affect the statistics of the examined plasma.

The kappa distributions have become increasingly widespread across space physics (for instance, ADS catalogs reveal an exponential growth of papers relevant to kappa distributions, e.g., Livadiotis & McComas 2013a). However, the vast majority of publications refer to various statistical fits and applications of kappa distributions in space plasmas. To date, there has been no analysis for verifying the origin of kappa distributions in the solar wind plasma. This paper identified three basic plasma conditions for the generation of kappa distributions in the solar wind near 1 au. Nevertheless, the presented results are preliminary as they have not yet been associated with the global interplanetary structures (e.g., corotating/stream interaction regions, shocks, and coronal mass ejections).

Finally, the paper evaluated the solar wind coupling and energization from a fundamental perspective, such as the nonequilibrium statistical mechanics. It addressed the mechanisms leading to the solar wind energy distribution during a time of preparation for Solar Probe and Solar Orbiter. The energy transfer that leads to the acceleration and heating of the solar wind is still under debate and will be addressed by unprecedented in situ observations close to the Sun in the near future.

The work was supported by the project NNX17AB74G of NASA's HGI Program.

## Appendix A Error Estimation

We describe the errors of (1) the parameters involved in the technique of deriving the kappa indices, (2) temperature

fluctuations, and (3) the plasma beta parameter. Equations are summarized in Table 2.

(1) *Kappa index ( $\kappa$ )*. It is derived from the ratio of thermal speeds,  $V_{\text{th,fit}}/V_{\text{th,mom}}$ , according to Equation (3) (e.g., Figure 6). The error of the ratio  $R = V_{\text{th,fit}}/V_{\text{th,mom}}$  is given by the propagation of the errors of  $V_{\text{th,fit}}$  and  $V_{\text{th,mom}}$ . The error  $\delta V_{\text{th,fit}}$  is given together with  $V_{\text{th,fit}}$  in the publicly accessible *Wind* data sets for solar wind plasma (Section 3.1); the error  $\delta V_{\text{th,mom}}$  is derived from  $\delta V_{\text{th,mom}}/V_{\text{th,mom}} = (1/2)\delta T/T \approx 0.04$  (because  $T$  is log-normally distributed with  $\delta T/T \approx \delta\ln T \approx 8\%$  for *Wind* SWE data, see Kasper et al. 2006); thus, we estimate the error  $\delta R$  in terms of the error  $\delta V_{\text{th,fit}}$ . Then, given the relation  $\kappa(R)$  in Equation (3), we derive the propagated error  $\delta\kappa$  in terms of the error  $\delta R$ .

(2) *Temperature fluctuations ( $\Delta T$ )*. This is given by  $\Delta T_i = |T_{i+1} - T_i|$  for the consecutive  $i$ th and  $(i+1)$ th data points. The propagation error is  $\delta\Delta T_i = \sqrt{\delta T_{i+1}^2 + \delta T_i^2}$  and because  $\delta\ln T = \delta T/T \approx 8\%$  (Kasper et al. 2006), we obtain  $\delta\Delta T_i = \sqrt{T_{i+1}^2 + T_i^2} \cdot 8\%$ .

(3) *Plasma beta ( $\beta$ )*. The plasma beta parameter is the ratio of the thermal to magnetic pressure,  $\beta \propto nT/B^2$ . Hence, its relative error is  $\delta\ln\beta = \delta\beta/\beta = \sqrt{(\delta\ln n)^2 + (\delta\ln T)^2 + 4(\ln B)^2}$ . The involved relative errors for temperature and density are  $\delta\ln T = \delta T/T \approx 8\%$  and  $\delta\ln n = \delta n/n \approx 3\%$ , respectively (Kasper et al. 2006). The relative error of the magnetic field strength is taken  $\delta\ln B = \delta B/B \approx 1\%$  (Lepping et al. 1995; Farrell et al. 1996). Thus, we find  $\delta\ln\beta \cong \sqrt{9 + 64 + 4\%} \cong 8.8\%$  or  $\delta\log\beta \approx 0.04$ .

## Appendix B Impact of Other Ion Populations

Here, we show that the contribution of other ion populations, such as alpha and pickup ions, in the proton temperature estimated by moments,  $T_{\text{mom}}$ , is insignificant and can be ignored.

We start with alpha particles. The mixing of non-equilibrium particle populations described by kappa distributions obeys the standard simple calorimetry rules (Livadiotis & McComas 2013a), so that  $T_{\text{mix}} = (n_p T_p + 4n_a T_a)/(n_p + 4n_a) \cong T_p + 4(n_a/n_p)T_a$ . On average,  $T_a \cong \frac{1}{4}T_p$  (Steinberg et al. 1996), hence, the temperature deviation  $\delta T_p = T_{\text{mix}} - T_p$  is given by  $\delta T_p/T_p \cong n_a/n_p$ . The ratio  $n_a/n_p$  is less than  $\sim 4\%$  for the fast wind and much less for the slow wind (Steinberg et al. 1996). Thus, we find that the temperature deviation due to alpha particles is less than  $\delta T_p/T_p \cong 4\%$ .

Similarly for the PickUp-Ion (PUI) population, we have a mixing temperature given by  $T_{\text{mix}} = (n_p T_p + n_{\text{PUI}} T_{\text{PUI}})/(n_p + n_{\text{PUI}}) \cong T_p + (n_{\text{PUI}}/n_p)T_{\text{PUI}}$ . Given that  $T_{\text{PUI}} \cong 10T_p$ , we find  $\delta T_p/T_p \cong 10(n_{\text{PUI}}/n_p)$ . The density ratio of PUI with protons is  $\sim 8\%$  at heliocentric distance  $r \sim 40$  au

(Richardson 1996) and  $\sim 6\%$  at  $r \sim 35$  au (Burlaga et al. 1994). Given that PUI density drops with  $\sim 1/r$  while proton density with  $\sim 1/r^2$ , we find that the ratio  $n_{\text{PUI}}/n_p$  at  $\sim 1$  au is less than 0.2%. This estimates the temperature deviation due to PUIs to be less than  $\sim 2\%$ .

Therefore, the ignorance of these two factors has small impact, because their contribution to the estimation of proton temperature is less than 4.5%, in total. Temperature values have already an error of about  $\sim 8\%$  and hardly can increase to 9% when implementing the calculated 4.5%.

## ORCID iDs

- G. Livadiotis <https://orcid.org/0000-0002-7655-6019>  
 M. I. Desai <https://orcid.org/0000-0002-7318-6008>  
 L. B. Wilson, III <https://orcid.org/0000-0002-4313-1970>

## References

- Abe, S. 1999, *PhyA*, **269**, 403  
 Abe, S. 2002, *PhyA*, **305**, 62  
 Baumjohann, W., & Treumann, R. A. 2012, Basic Space Plasma Physics, Revised and Extended (London: Imperial College Press)  
 Beck, C., & Cohen, E. G. D. 2003, *PhyA*, **322**, 267  
 Bryant, D. A. 1996, *JPIPh*, **56**, 87  
 Burlaga, L. F., Ness, N. F., Belcher, J. W., et al. 1994, *JGR*, **99**, 21511  
 Collier, M. R., Hamilton, D. C., Gloeckler, G., Bochsler, P., & Sheldon, R. B. 1996, *GeoRL*, **23**, 1191  
 Farrell, W. M., Fitznerreiter, R. J., Owen, C. J., et al. 1996, *GeoRL*, **23**, 1271  
 Fisk, L. A., & Gloeckler, G. 2014, *JGR*, **119**, 8733  
 Fuselier, S. A., Allegrini, F., Bzowski, M., et al. 2014, *ApJ*, **784**, 89  
 Gougam, L. A., & Tribeche, M. 2011, *PhPl*, **18**, 062102  
 Grassi, A. 2010, *IJQC*, **111**, 2390  
 Jian, L., Russell, C. T., Luhmann, J. G., Galvin, A. B., & MacNeice, P. J. 2009, *SoPh*, **259**, 345  
 Jian, L., Russell, C. T., Luhmann, J. G., & Skoug, R. M. 2006a, *SoPh*, **239**, 393  
 Jian, L., Russell, C. T., Luhmann, J. G., & Skoug, R. M. 2006b, *SoPh*, **239**, 337  
 Jund, P., Kim, S. G., & Tsallis, C. 1995, *PhRvB*, **52**, 50  
 Kallenrode, M.-B. 2004, Space Physics: An Introduction to Plasmas and Particles in the Heliosphere and Magnetospheres (Berlin: Springer)  
 Kartalev, M., Dryer, M., Grigorov, K., & Stoimenova, E. 2006, *GeoRL*, **111**, A10107  
 Kasper, J. C., Lazarus, A. J., Steinberg, J. T., Ogilvie, K. W., & Szabo, A. 2006, *JGR*, **111**, A03105  
 King, J. H., & Papitashvili, N. E. 2005, *JGR*, **110**, 2104  
 Kivelson, M. G., & Russell, C. T. 1995, Introduction to Space Physics (Cambridge: Cambridge Univ. Press)  
 Lepping, R. P., Acuna, M. H., Burlaga, L. F., et al. 1995, *SSRv*, **71**, 207  
 Lin, R. P., Anderson, K. A., Ashford, S., et al. 1995, *SSRv*, **71**, 125  
 Livadiotis, G. 2007, *PhyA*, **375**, 518  
 Livadiotis, G. 2012, *Entrp*, **14**, 2375  
 Livadiotis, G. 2015a, *JGRA*, **120**, 1607  
 Livadiotis, G. 2015b, *Entrp*, **17**, 2062  
 Livadiotis, G. 2015c, *JGRA*, **120**, 880  
 Livadiotis, G. 2015d, *JPCS*, **577**, 012018  
 Livadiotis, G. 2016, *ApJS*, **223**, 13  
 Livadiotis, G. 2017, Kappa Distribution: Theory Applications in Plasmas (1st ed.; Netherlands: Elsevier)  
 Livadiotis, G., Assas, L., Dennis, B., Elaydi, S., & Kwessi, E. 2016, *Nat. Res. Mod.*, **29**, 130  
 Livadiotis, G., & Desai, M. I. 2016, *ApJ*, **829**, 88  
 Livadiotis, G., & McComas, D. J. 2009, *JGRA*, **114**, 11105  
 Livadiotis, G., & McComas, D. J. 2010a, *ApJ*, **714**, 971  
 Livadiotis, G., & McComas, D. J. 2010b, *PhyS*, **82**, 035003  
 Livadiotis, G., & McComas, D. J. 2011a, *ApJ*, **738**, 64  
 Livadiotis, G., & McComas, D. J. 2011b, *ApJ*, **741**, 88  
 Livadiotis, G., & McComas, D. J. 2012, *ApJ*, **749**, 11  
 Livadiotis, G., & McComas, D. J. 2013a, *SSRv*, **75**, 183  
 Livadiotis, G., & McComas, D. J. 2013b, *Entrp*, **15**, 1118  
 Livadiotis, G., & McComas, D. J. 2014a, *JPIPh*, **80**, 341  
 Livadiotis, G., & McComas, D. J. 2014b, *JGRA*, **119**, 3247  
 Livadiotis, G., McComas, D. J., Dayeh, M. A., Funsten, H. O., & Schwadron, N. A. 2011, *ApJ*, **734**, 1  
 Livadiotis, G., McComas, D. J., Randol, B., et al. 2012, *ApJ*, **751**, 64  
 Livadiotis, G., McComas, D. J., Schwadron, N. A., Funsten, H. O., & Fuselier, S. A. 2013, *ApJ*, **762**, 134  
 Maksimovic, M., Pierrard, V., & Riley, P. 1997, *GeoRL*, **24**, 1151  
 Mann, G., Classen, H. T., Keppler, E., & Roelof, E. C. 2002, *A&A*, **391**, 749  
 Marsch, E. 2006, *LRSP*, **3**, 1  
 Meyer-Vernet, N., Moncuquot, M., & Hoang, S. 1995, *Icar*, **116**, 202  
 Murawski, K., Nakariakov, V. M., & Pelinovsky, E. N. 2001, *A&A*, **366**, 306  
 Nakariakov, V. M., & Roberts, B. 1995, *SoPh*, **159**, 213  
 Nakariakov, V. M., Roberts, B., & Mann, G. 1996, *A&A*, **311**, 311  
 Narita, Y., Gary, S. P., Saito, S., Glassmeier, K.-H., & Motschmann, U. 2011, *GeoRL*, **38**, L05101  
 Nicolaou, G., & Livadiotis, G. 2016, *Ap&SS*, **361**, 359  
 Nicolaou, G., Livadiotis, G., & Moussas, X. 2014, *SoPh*, **289**, 1371  
 Ogasawara, K., Angelopoulos, V., Dayeh, M. A., et al. 2013, *JGR*, **118**, 3126  
 Ogasawara, K., Livadiotis, G., Grubbs, G. A., et al. 2017, *GeoRL*, **44**, 3475  
 Ogilvie, K. W., Chornay, D. J., Fritzenreiter, R. J., et al. 1995, *SSRv*, **71**, 55  
 Pascoe, D. J., Nakariakov, V. M., & Kupriyanova, E. G. 2014, *A&A*, **568**, A20  
 Pavlos, G. P., Malandraki, O. E., Pavlos, E. G., Iliopoulos, A. C., & Karakatsanis, L. P. 2016, *PhyA*, **464**, 149  
 Pierrard, V., & Lazar, M. 2010, *SoPh*, **267**, 153  
 Pierrard, V., Maksimovic, M., & Lemaire, J. 1999, *JGR*, **104**, 17021  
 Pierrard, V., & Pieters, M. 2015, *JGR*, **119**, 9441  
 Rajagopal, A. K. 2006, arXiv:cond-mat/0608679  
 Richardson, J. D. 1996, in Physics of Space Plasmas, ed. T. Chang & J. R. Jasperse (Cambridge, MA: MIT Press), 431  
 Roberts, B. 1991, in Advances in Solar System Magnetohydrodynamics, ed. E. R. Priest & A. W. Hood (Cambridge: Cambridge Univ. Press), **105**  
 Roberts, B., & Ulmschneider, P. 1997, *LNP*, **489**, 75  
 Rubab, N., & Murtaza, G. 2006, *PhyS*, **74**, 145  
 Salazar, R., & Toral, R. 1999, *PRL*, **83**, 4233  
 Schwadron, N. A., Dayeh, M. A., Desai, M., et al. 2010, *ApJ*, **713**, 1386  
 Shestov, S., Nakariakov, V., & Kuzin, S. 2015, *ApJ*, **814**, 135  
 Steinberg, J. T., Lazarus, A. J., Ogilvie, K. W., Lepping, R., & Byrnes, J. 1996, *GeoRL*, **23**, 1183  
 Stepanova, M., & Antonova, E. E. 2015, *JGR*, **120**, 3702  
 Štverák, S., Maksimovic, M., Travnicek, P. M., et al. 2009, *JGR*, **114**, A05104  
 Sunjung, K., Yoon, P. H., Choe, G. S., & Wang, L. 2015, *ApJ*, **806**, 32  
 Tao, X., & Lu, Q. 2014, *PhPl*, **21**, 022901  
 Tirmakli, U., & Borges, E. P. 2016, *Sci Rep.*, **6**, 23644  
 Touchette, H. 2004, in Nonextensive Entropy—Interdisciplinary Applications, ed. M. Gell-Mann & C. Tsallis (Oxford: Oxford Univ. Press), 159  
 Tsallis, C. 2009, Introduction to Nonextensive Statistical Mechanics (New York: Springer)  
 Vignat, C., Plastino, A., & Plastino, A. R. 2005, *NCimB*, **09**, 951  
 Villain, J. 2008, *Sci. Acta*, **2**, 93  
 Wilson, L. B., Sibeck, D. G., Breneman, A. W., et al. 2014a, *JGR*, **119**, 6455  
 Wilson, L. B., Sibeck, D. G., Breneman, A. W., et al. 2014b, *JGR*, **119**, 6475  
 Wilson, L. B., III, Cattell, C. A., Kellogg, P. J., et al. 2010, *JGR*, **115**, A12104  
 Yoon, P. H. 2014, *JGR*, **119**, 7074  
 Yoon, P. H., Ziebell, L. F., Gaelzer, R., Lin, R. P., & Wang, L. 2012, *SSRv*, **173**, 459  
 Zank, G. P., Li, G., Florinski, V., et al. 2006, *JGR*, **111**, A06108  
 Zouganelis, I. 2008, *JGR*, **113**, A08111